Lab on a Chip

PAPER

View Article Online
View Journal

Cite this: DOI: 10.1039/d4lc00087k

Investigation of air bubble behaviour after gas embolism events induced in a microfluidic network mimicking microvasculature†

Mohammad Mahdi Mardanpour, ‡[a] Ayyappasamy Sudalaiyadum Perumal, ‡[a] Zahra Mahmoodi,[a] Karine Baassiri,[a] Gala Montiel-Rubies,[a] Kenneth M. LeDez[b] and Dan V. Nicolau *[a]

Gas embolism is a medical condition that occurs when gas bubbles are present in veins or arteries, decreasing blood flow and potentially reducing oxygen delivery to vital organs, such as the brain. Although usually reported as rare, gas embolism can lead to severe neurological damage or death. However, presently, only limited understanding exists regarding the microscale processes leading to the formation, persistence, movement, and resolution of gas emboli, as modulated by microvasculature geometrical features and blood properties. Because gas embolism is initially a physico-chemical-only process, with biological responses starting later, the opportunity exists to fully study the genesis and evolution of gas emboli using *in vitro* microfluidic networks mimicking small regions of microvasculature. The microfluidics networks used in this study, which aim to mimic microvasculature geometry, comprise linear channels with T-, or Y-junction air inlets, with 20, 40, and 60 μm widths (arterial or venous), and a 30 μm width honeycombed network (arterial) with three bifurcation angles (30°, 60°, and 90°). Synthetic blood, equivalent to 46% haematocrit concentrations, and water were used to study the modulation of gas embolism-like events by liquid viscosity. Our study shows that (i) longer bubbles with lower velocity occur in narrower channels, *e.g.*, with 20 μm width; (ii) the resistance of air bubbles to the flow increases with the higher haematocrit concentration; and lastly (iii) the propensity of gas embolism-like events in honeycomb architectures increases for more acute, *e.g.*, 30°, bifurcation angles. A dimensionless analysis using Euler, Weber, and capillary numbers demarcated the conditions conducive to gas embolism. This work suggests that *in vitro* experimentation using microfluidic devices with microvascular tissue-like structures could assist medical guidelines and management in preventing and mitigating the effects of gas embolism.

Received 28th January 2024,
Accepted 31st March 2024

DOI: 10.1039/d4lc00087k

rsc.li/loc

1 Introduction

Gas embolism is an emergency medical condition occurring when intravascular gas bubbles result in restricted or obstructed blood and oxygen supply to the brain or other vital organs.[1] Gas bubbles are either intentionally or accidentally introduced into the vascular system during invasive medical procedures,[2] or produced as a result of decompression illnesses.[3] Although reported as rare, gas embolism can be unsuspected or undiagnosed, with critical medical outcomes including severe neurological damage or death.[4] Depending on the localization of the gas bubble, gas embolism can be venous (VGE),[5] or arterial (AGE).[6] Bubbles present in the venous system can breach through the lung bubble filter, or otherwise can reach the arterial circulation, *e.g.*, *via* patent foramen ovale (PFO), and they may lead to AGE or cerebral arterial gas embolism (CAGE). Other vital tissues may also become ischemic,[7] including the cerebral and spinal cord, leading to neurological issues or due to coronary artery gas embolism, leading to cardiac arrest.

Gas embolism can occur *via* the localised creation of gas emboli during medical surgeries, *e.g.*, inadvertent or intentional infusion of gas bubbles and exposure to compressed gas used in a variety of techniques, such as laparoscopy,[8] peripheral[9,10] or central venous[11,12] catheterizations, hysteroscopic endometrial ablation,[13,14] cardiopulmonary bypass, resuscitations,[15] neurosurgery,[16] endoscopies,[17] haemodialysis,[18] and during wound irrigation with hydrogen peroxide.[19] A study on the incidence of gas

[a] Department of Bioengineering, Faculty of Engineering, McGill University, Montreal, Québec, H3A 0E9, Canada. E-mail: dan.nicolau@mcgill.ca
[b] Faculty of Medicine, Health Sciences Centre, Memorial University, St. John's, Newfoundland and Labrador, A1C 5S7, Canada

† Electronic supplementary information (ESI) available: For additional data, figures, and detailed methods related to the experiments and findings discussed in this article, supporting information was provided. See DOI: https://doi.org/10.1039/d4lc00087k

‡ These authors contributed equally to this work.

embolism in hospital environments during surgeries reported high mortality rates, of up to 21%.[4]

Alternatively, gas embolism can occur globally due to the reduction of pressure (decompression) experienced by the whole body, for instance occasioned by deep-sea diving or high altitude and aerospace operations, with the classical case being[20] decompression sickness (DCS). CAGE constitutes the second most significant category of fatalities, accounting for 13–24% of cases among divers.

Pulmonary barotrauma caused by blast or penetrating trauma is a case in between local and global gas embolism, where the variation of pressure is focused on a particular organ, such as the lung.[21]

Presently, the morbidity and mortality of gas embolism cannot be accurately quantified due to the high complexity of reported cases, possibly coupled with underreporting. However, based on retrospective studies, it was established that gas embolism is one of the major critical issues in intensive care units.[22,23] While the incidence and the outcomes of gas embolism were comprehensively reported,[24] only a few recent studies[25–29] explored the dynamics of the bubble behaviour physically simulated by *in vitro* experiments. The studies explored the behaviour of gas bubbles in PDMS-based microchannels under different flow properties like gas bubble behaviour in low capillary number microchannels;[26] roles of the cell-free layer and cell local concentration in the persistence of the bubble;[25] impacts of the T-junction on bubble break-up;[27] flow of blood cells around the bubble in PDMS-fabricated blood vessels;[28] and use of microfluidic devices for studying cellular responses to gas embolism.[29]

Advances in microfluidic technology facilitated novel ways of studying complex physiochemical and biological phenomena in live tissues.[30,31] Microfluidic devices are often fabricated using polydimethylsiloxane (PDMS),[32] including those for studies related to gas embolism.[25,26,28] PDMS is an elastomeric polymer with well-established microfabrication protocols[33] and many essential properties, *e.g.*, good optical transparency,[34] high replication precision by soft lithography,[32] and biological compatibility for cell studies.[35] Regarding its suitability for mimicking blood vessel tissue, the Young's modulus of PDMS usually ranges from 0.05 to 2 MPa,[36] and up to 5 MPa,[37] compared with 0.04 to 2 MPa for sections of the human abdominal aorta, 0.05 to 1.45 MPa for the human iliac artery,[38] and up to 5 MPa for cerebral arteries.[39] PDMS also presents similar oxygen diffusivity with blood vessels,[40] which is another important consideration. Consequently, PDMS-based microfluidics technology offers a versatile tool for the exploration of *in vitro* gas embolism.[28,41–43]

The displacement of exogenously introduced bubbles and their evolution was studied[25] using fluids with two haematocrit concentrations (5% and 10%) flowing in microfluidic devices with two levels of bifurcation, which led to an asymmetric division of the air bubbles. Recently, an *in vitro* microfluidics-based investigation[28] detailed the environment around gas emboli and clot formation, as well as investigating the formation of Taylor bubbles (elongated bubbles) in a serpentine channel with T-junctions.

Regardless of the genesis of gas embolism, that is, local or global variation of pressure generated *in situ* accidentally or intentionally introduced in the blood flow, in all instances, the medical consequences are the result of the microscale evolution of the lengths, the position, and the flow behaviour of gas bubbles in the vascular system. Acknowledging this generality of post-genesis processes, we studied the evolution of gas bubbles after gas embolism-like initiation by injecting air in microfluidic networks mimicking the microvasculature system. This work explored the influence of input parameters, *i.e.*, channel widths and geometries, fluid parameters, *e.g.*, haematocrit concentration and surface tension, air-to-liquid ratios (namely air volume/liquid volume), and liquid flow rate, on the output parameters of gas embolism, namely, the length and velocity of air bubbles, their stability, and the potential restriction of flow in blood vessels. The study provides insights into the medical relevance of the observed results.

2 Materials and methods

2.1 Microfluidic chips and overall experimental setup

The experimental setup with various channel geometries mimicking microvasculature is presented in Fig. 1. The linear channels with T- and Y-junction inlets and widths of 20 μm, 40 μm, and 60 μm were used to investigate slug flows. The effects of the air-to-liquid mixing interface, the liquid slug sizes, and the parameters of air bubbles, *i.e.*, velocity and displacement, were measured (Fig. 1D). The honeycomb-shaped network with 30 μm width channels and three different bifurcation angles *i.e.*, 30°, 60°, and 90° (Fig. 1B, C and S1†), resulting in six bifurcation generations, was used to assess the impact of the bifurcation angle on the bubble behaviour like displacement and blockage in the channels.

Standard SU-8 photolithography was used to fabricate the masters, followed by PDMS soft lithography replication (fabrication protocol detailed in ESI,† Fig. S2). The devices were treated with oxygen plasma and sealed on clean glass slides. The experimental setup used programmable syringe pumps (Pump 11 Elite Syringe Pumps, Harvard Apparatus) to inject different fluids into the microfluidic networks. An inverted confocal microscope (Olympus IX83 fluorescence microscope, Olympus Corporation) coupled with a high-speed camera (C11440-42U30, Hamamatsu Photonics K.K.) was used for visualization. All experiments were imaged using a UPlano 1.25× magnifying objective. The images were acquired at the mid-plane of the microfluidic chips at a frame rate of 250 frames per second (fps). The maximum field of view obtained with this system was 143.2 mm^2.

2.2 Working fluids

The two fluids used in this study vary in viscosity and surface tension tailored to match the rheological properties of blood at 46% haematocrit concentrations. Demineralized water was

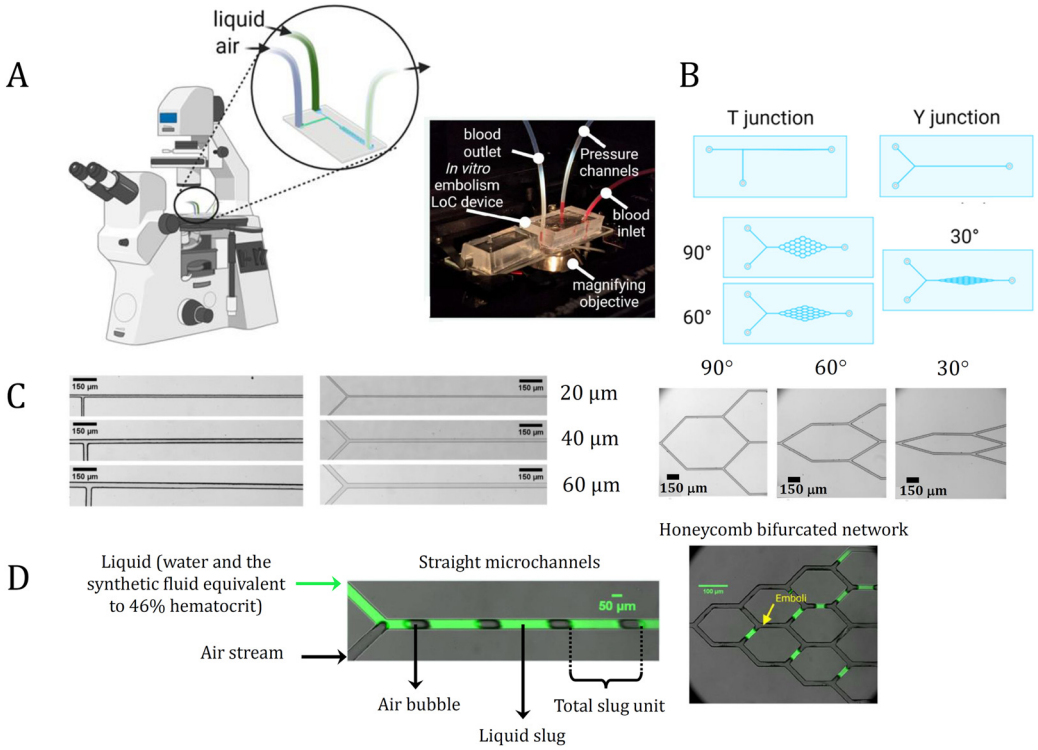

Fig. 1 Experimental setup and microvascular-mimicked architectures used to study gas embolism in different microfluidic structures mimicking blood vessels. (A) The experimental setup includes a microscope (Olympus IX83) and the microfluidic device (in the inset) with inlets for air (in blue) and fluorescent liquid (in green), outlet (in light green). The inlets are connected to programmable syringe pumps. (B) Overall and (C) partial optical images of the microvasculature structures used for studying the parameters that modulate gas embolism *in vitro*. (D) The schematics showing the inlets, the working fluids used in this study, the lengths of air bubbles, liquid slugs and total slug units and their boundaries for the T- and Y-junction channels. Additionally, the trapped bubbles and liquid slugs inside the honeycomb bifurcated network were shown.

used as a control, equivalent to 0% haematocrit concentration. The synthetic blood formulation consisted of 60% water, 40% glycerin, and a varying total amount of xanthan gum to mimic blood viscosities and its surface tension (0.04% for the synthetic blood).[44,45] The viscosity and surface tension properties of the synthetic haematocrit preparations and animal blood samples were measured using a rheometer (Anton Paar MCR302 Rheometer) and goniometer (RameHart 90). The results of the measurements and relevant discussion are provided in the ESI† (Tables S1 to S3 and Fig. S3). The liquid flow rates in the microvasculature were similar to the blood flow in human arterioles.[46] For the 20, 30, 40, and 60 µm channels, the liquid flow rates were 12, 24, 42, and 90 µl h^{-1}, respectively. The air-to-liquid ratio was selected between 10 and 100, based on the least value at which the bubbles could enter the liquid flow in the channel and the maximum at which the airflow completely stopped the flow of the liquid, respectively. The pressure of the injected air into the channels was measured by a microfluidic in-line pressure sensor (Fluigent Company Inc., USA), with a pressure range of −1000 to 7000 mbar. The liquid was not recirculated but collected after flowing through the microfluidic network. For high-quality image analysis, a green fluorescence tracer, fluorescein, was mixed with the working fluid (1 ml of 2% stock solution for 50 ml working fluid) to track the movement of the liquid slugs and total slugs.

2.3 Image analysis

ImageJ FIJI software was used to process the recorded images of the fluid operation in the microfluidic devices. Several image analysis parameters were measured, *i.e.*, length, velocity, and retention time of the air bubbles and liquid slugs. The quantitative data analysis was performed using in-house developed MATLAB codes to identify the liquid slugs and air bubbles based on fluorescence intensity, using 8-bit microscopy images converted to binary images based on protocols reported elsewhere.[47] Two analyses, namely density maps and median analysis, were used for mapping the dynamic locations and the stagnant or blocked features in the network, respectively. Microsoft Excel and MATLAB-based graph plotting tools were used to plot the datasets. The median analysis and density maps were generated based on the protocol discussed in previous studies.[48]

3 Results and discussion

3.1 Flow patterns of fluids in the channels

Four typical flow patterns were observed, modulated by (i) the geometries of the microfluidic systems, *i.e.*, channel widths, T-,

or Y-junctions, and (ii) fluid properties, *i.e.*, air-to-liquid ratios (namely air volume/liquid volume), equivalent concentrations of haematocrit and surface tension (presented in Fig. 2, and Movie S1†). The green fluorescence in the microscopy images represents the liquid, while non-fluorescent areas represent gas bubbles. Movie S1 (ESI†) presents typical experimental results with different slug flows. Slug flow (or Taylor flow) is defined as the successive displacement of a total slug unit composed of an air bubble and a liquid phase known as the liquid slug.[49] The flow patterns and their respective fluorescence intensity plots in the channels, presented in Fig. 2A and B, presented the following characteristics:

(i) Continuous flow of a single liquid phase was predominant for low air-to-liquid ratios, especially below 10, both for water and for synthetic blood. During the continuous flow pattern, air bubbles were not formed regularly but only as intermittent random bubbles (Fig. 2A).

(ii) Liquid-dominated, recurrent air-in-liquid slug flow (Fig. 2B and C) presented bubbles of varying lengths and spacing in the liquid-dominated regime, which occurs when the channels are predominantly occupied by liquid with only occasional bubbles. The variant presenting long liquid slugs occurred in synthetic blood and, in most cases, for the flow in 20 μm channels.

(iii) Air-dominated, recurrent liquid-in-air bubble flow (Fig. 1D) occurred predominantly for the water in networks with T-junctions (irrespective of the air-to-liquid ratios) and Y-junctions at air-to-liquid ratios above 20 and above 30 for synthetic blood. The length of the liquid slugs was smaller than the length of the air bubbles.

(iv) Stratified, continuous flow (Fig. 2E) was observed in channels with Y-junctions for water and synthetic blood when the liquid and the air flowed smoothly as a continuous two-phase parallel flow. A higher air-to-liquid ratio translated into a higher portion of air volume occupying the channel cross-section and the thinning of the liquid layers.

The length and velocity of air bubbles and liquid slugs were used to quantitatively assess the effects of an equivalent concentration of haematocrit, channel width, junction type, and air-to-liquid ratio on the flow patterns and on the physical parameters of the liquid slug and air bubble (total slug).

3.2 Parameters of the air bubble displacement in T- and Y-junction linear channels

Three parameters of the flow in channels with T- and Y-junctions, namely (i) channel width, (ii) equivalent concentration of haematocrit (and associated surface tension), and (iii) air-to-liquid ratios, impacted the parameters and the bubbles. The microscopy image panel for varying flow patterns for all air-to-liquid flow ratios, ranging from 10 to 100, for both junction types and for all fluids with haematocrit equivalent concentrations, are presented in ESI† Fig. S4 to S6.

3.2.1 Variation of the bubble length in channels with T- and Y-junctions. The evolution of air pressure, continuously recorded during the experiments, presented two regimes: (i) a ramp-up of the pressure and (ii) a quasi-steady state regime, both with variations around the base lines (data presented in ESI,† Fig. S7 to S13). Because our study is focused on the evolution of gas bubbles once they are present in the mimicked microvasculature, further analysis referred to the stabilized region of the pressure drop. In this regime, two distinct distributions of the lengths of bubbles and total slugs were observed: (i) flow with uniform bubbles and (ii) flow with

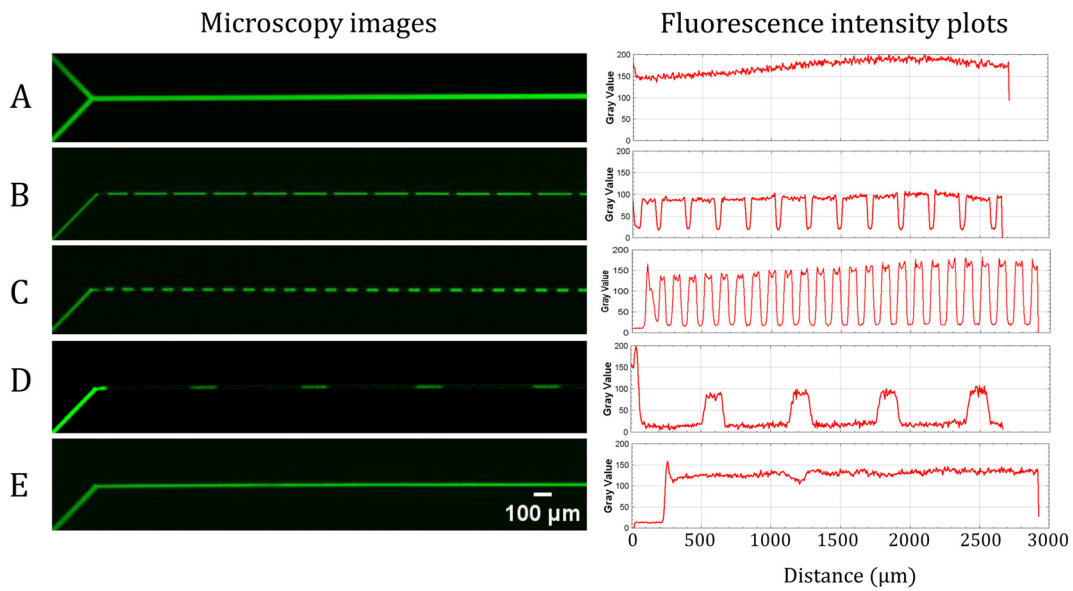

Fig. 2 The flow patterns in different microfluidic structures mimicking blood vessels. (A) Continuous flow (single liquid phase flow). (B) and (C) Liquid-dominated pattern, repetitive air bubbles in liquid slug flow, with different dimensions and frequencies. (D) Air-dominated pattern, liquid in air bubble flow. (E) Stratified behaviour, continuous laminar flow. Slug flow patterns were observed in (B)–(D). The intensity plot profile compares the intensity of fluorescence spikes due to the different flow patterns in the channels.

non-uniform bubbles. A coefficient of variation less than 10% characterizes the flow pattern as the flow with uniform bubbles, while a higher coefficient of variation designates the flow with non-uniform bubbles. Movie S2† presents the microscopy imaging of these two distributions for the respective air-to-liquid ratios. For uniformly sized total slugs, the air bubbles and liquid slugs traversed the channel without a significant difference in the length of the moving bubbles or liquid slugs. This pattern was observed in most air-to-liquid ratios for flows in 20 μm channels. For 40 and 60 μm channels, the flow with uniform bubbles occurred just in a few instances when the air-to-liquid ratios were lower (Fig. S5 and S6†). For higher air-to-liquid ratios in the Y-junction, the flow with non-uniform bubbles was observed (Fig. S4 to S6†).

Fig. 3A to D represent the average values and the standard deviations of bubble length in channels with T- and Y-junctions for various air-to-liquid ratios, as derived from independent experiments ($1700 \leq n \leq 44\,000$ measurements of bubbles for water, and $3500 \leq n \leq 198\,000$ measurements of bubbles for synthetic blood). Irrespective of the junction type and fluid viscosity, the bubble lengths in channels with 20 μm widths were longer than those in 40 μm channels (Fig. 3A and B). An increase in fluid viscosity resulted in a decrease in the average bubble length (Fig. 3C and D). The standard deviations of the bubble lengths in channels with Y-junctions were higher than those for channels with T-junctions, as previously reported.[50] The 60 μm channels with Y-junctions (Fig. 3B and D) exhibited a stratified flow for all air-to-liquid ratios, except for the water at the air-to-liquid ratios of 1 : 10 and 1 : 20. The ascending linear trend of the bubble size for all channel widths, junction types, and fluid viscosity suggests that an increase in the air-to-liquid ratio will result in an increase in the bubble length (with water flow in 20 μm channels exhibiting a steeper increase *vs.* air-to-liquid ratios). For the flow with uniform bubbles, the length of air bubbles for the Y-junctions is shown in the inset of Fig. 3C and D, respectively. In this case, the length of the air bubbles in 40 μm channels was longer than that for 20 μm channels. Also, as expected, by increasing the air-to-liquid ratios, the length of the air bubbles increased as well. These observations correlate well with other studies.[51] It is noteworthy that the trend in air bubble length closely aligns with the trend in liquid slug length across all scenarios, for channels with T- and Y-junctions, with varying air-to-liquid ratios, and for both water and synthetic blood (ESI,† Fig. S14).

3.2.2 Variation of the bubble velocity in channels with T- and Y-junctions. The velocity of the air bubbles in the channels is presented in Fig. 3E to H. The injection rates of the liquid into the channel were comparable with the average flow rates in arterioles and venules,[46] *i.e.*, 12, 42, and 90 μl h^{-1} for the channel widths of 20, 40 and 60 μm, respectively. The bubble velocities in wider channels were higher than those in the narrower ones due to higher fluid flow resistance in channels with smaller widths. Irrespective of the junction type

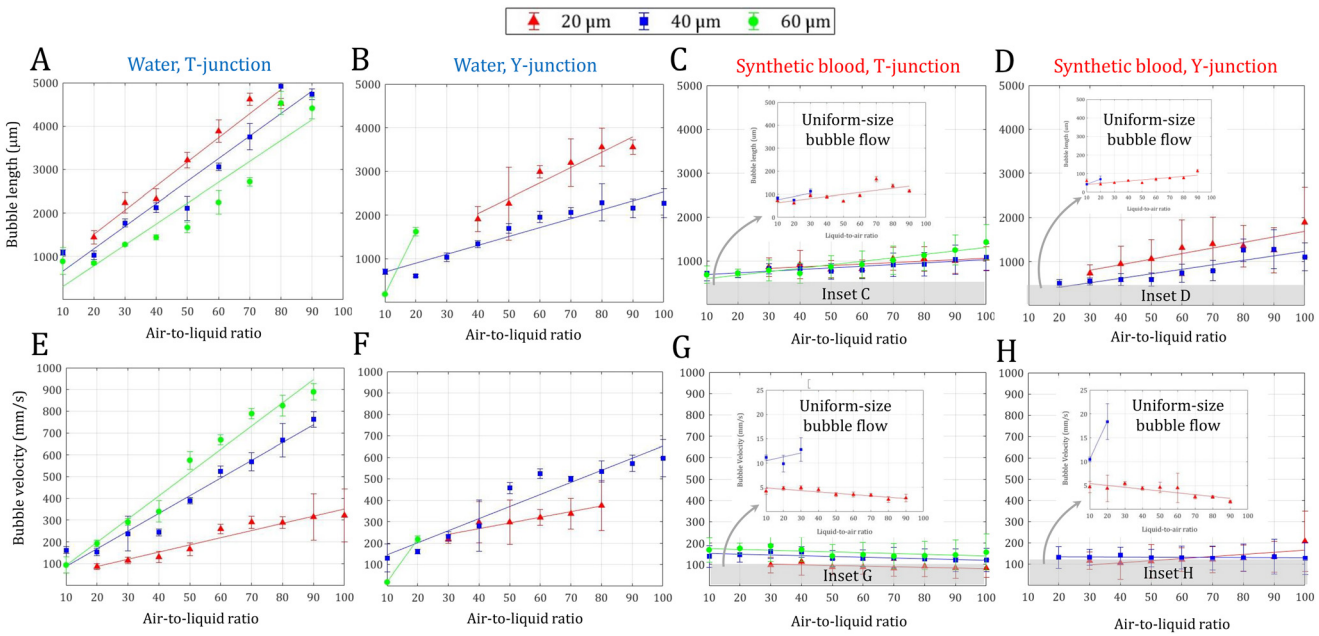

Fig. 3 Graphs of the measured lengths of air bubbles across different air-to-liquid ratios for the (A) water, T-junction, (B) synthetic blood, T-junction, (C) water, Y-junction and (D) synthetic blood, Y-junction. The inset of Fig. 3C and D display the length of air bubbles for the flow with uniform bubbles in synthetic blood at T and Y-junctions, respectively. The standard deviation represents the length variation of the air bubbles calculated from the observed values in linear channels, with larger values representing larger fluctuations in the length of air bubbles. Effect of the junction type, channel width, air-to-liquid ratio, and liquid viscosity on the velocity of the air bubbles for (E) water at T-junction channel; (F) synthetic blood at T-junction channel; (G) water at Y-junction channel; and (H) synthetic blood at Y-junction channel. Inset Fig. 3G and H depict the velocity of uniform bubbles in synthetic blood at T and Y-junctions, respectively. The standard deviation represents the velocity variation of the air bubbles calculated from the observed values in linear channels, with larger values representing larger fluctuations in the velocity of air bubbles.

and liquid viscosity, the velocity of bubbles inside 60 μm channels was the highest, followed by 40 and 20 μm channels. For synthetic blood, the stratified flow pattern persisted for all air-to-liquid ratios. As expected, an increase in fluid viscosity translates into increased hydraulic resistance and, consequently, a decrease in fluid velocity (Fig. 3G and H). In addition, Fig. 3E and F show that for water, an increase in the air-to-liquid ratio significantly increased the velocity of the bubbles, but for the synthetic blood, there was no pronounced variation in bubble velocity (Fig. 3G and H). For the flow with uniform bubbles (inset Fig. 3G and H), although the velocity of the bubbles inside the 40 μm channels was remarkably higher than that for the 20 μm channels, an increase in the air-to-liquid ratio did not result in an increase in bubble velocity. Finally, the bubble velocities in channels with T-junctions were marginally lower than those in channels with Y-junctions, irrespective of liquid viscosity.

The fluctuations of velocities of the fluid and of the bubbles were modulated by the channel width, viscosity, and air-to-liquid flow ratio, as shown by their respective standard deviations in Fig. 3E to H. The transition from the "air in liquid" flow pattern to the "liquid in air" pattern (Fig. 2) led to an increased variation in the lengths of liquid slugs and air bubbles. The variation observed in the lengths of the liquid slugs due to this transition was also reported elsewhere.[43,52–54]

From the analysis of the effect of junction types, it appeared that the preconditions leading to gas embolism-like events, *i.e.*, a non-uniform alternating behaviour, frequent halting of the air bubbles, and higher resistance of air bubbles to flow, were more prevalent in narrower channels, *e.g.*, with 20 μm widths, than in other channels used in this study.

3.2.3 Distributions of bubble lengths. Fig. 4 presents the distributions of bubble lengths in channels with T- (Fig. 4A and B) and Y-junctions (Fig. 4C and D) for selected air-to-liquid ratios. The full description of histogram charts for all channel widths, air-to-liquid ratios, and working fluids is presented in the ESI,† Fig. S15 to S20.

Fig. 4A shows that an increase in the air-to-liquid ratios led to longer bubbles. Expectedly, smaller channel widths translated into longer bubble lengths, with this trend being linearly dependent on the channel width. This relationship was observed for water flowing in channels with Y-junctions (Fig. 4C, further illustrated for the entire panel of tested conditions in Fig. S16 and S17†).

As can be observed in Fig. 4B and D (for synthetic blood), for channels with both T- and Y-junctions, an increase in the air-to-liquid ratio did not translate into a significant shift towards longer bubbles. Apparently, an increase in the liquid viscosity translated into an increase in the hydraulic resistance, and the formation of longer bubbles in the channel required higher air pressure. Fig. S18 to S20† show this feature for all values of air-to-liquid ratios.

The distribution of the length of air bubbles in channels with T-junctions was more uniform than those in channels with Y-junctions, especially for 20 μm channels (Fig. 4). Additionally, the distributions of the bubble sizes in the

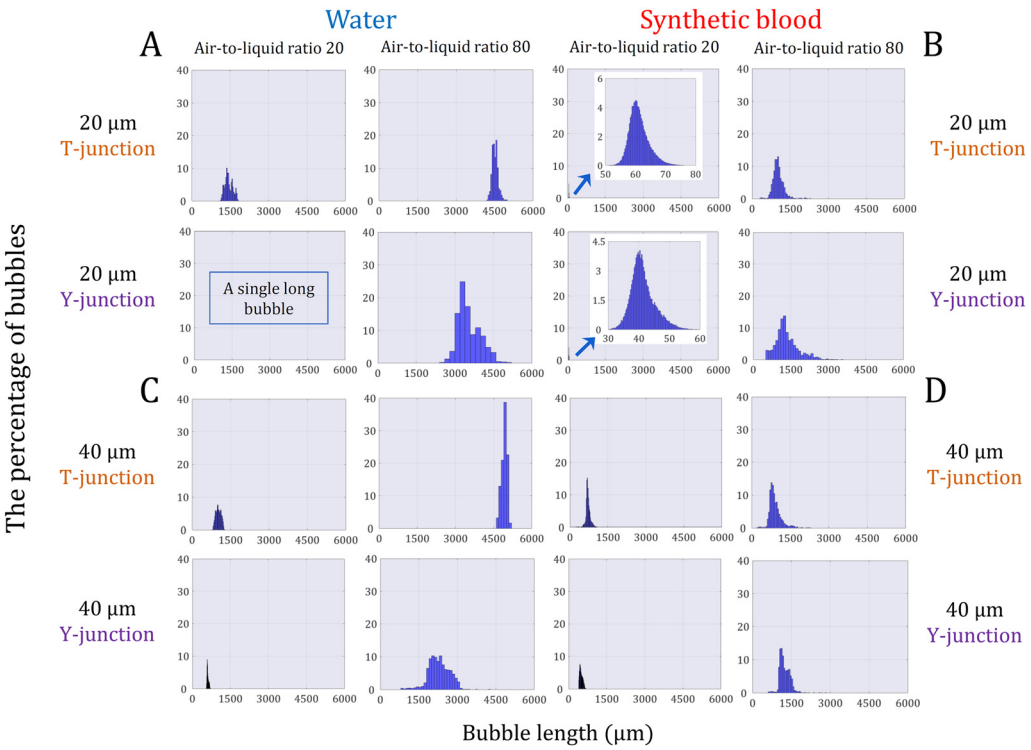

Fig. 4 The histograms and variation of the bubble length in linear channels for different air-to-liquid ratios. Histogram of bubble length for the (A) water, T-junction, (B) synthetic blood, T-junction, (C) water, Y-junction, and (D) synthetic blood, Y-junction in air-to-liquid ratios of 20 and 80 for different channel widths. The full description of histogram charts for all air-to-liquid ratios is presented in the ESI† (Fig. S12 to S19).

channels with T-junctions were more normally symmetrical than those for the channels with Y-junctions (ESI,† Fig. S15).

The bubble generation process comprised an initial phase in which the dimensions of the bubbles were uneven (unstable bubble generation phase), followed by a phase in which bubbles presented similar sizes (stable bubble generation phase). In the stable bubble generation phase, bubbles maintained their shape, resulting in a normal distribution of bubble lengths. Conversely, the unstable bubble generation involved the breakup of some bubbles, leading to varying sizes and a non-normal distribution of bubble lengths. This phenomenon was particularly noticeable at high Reynolds and capillary numbers, indicating an imbalance between the inertial and the viscous forces, as well as between the viscous force and the interfacial tension, respectively. Consequently, the normal distribution of bubble lengths in Fig. 4 is the result of the balance of dominant forces, as reported elsewhere.[55] Fig. S21 and S22† illustrate the 3D histograms representing air bubble volume in relation to the injected air pressure.

3.2.4 Dimensionless numbers predicting the preconditions for the high-risk of gas embolism. The central motivation of our study was to be able to predict the conditions under which gas embolism is likely to occur. To progress on the understanding of the modulation of gas embolism by channel geometries, fluid properties, and air-to-liquid ratios, the results of *in vitro* experiments must be used as inputs to a dimensionless analysis of the balance between the forces that can lead to channel blockage by air bubbles, that is, the inertial force, the pressure force, the viscous force, and the interfacial force.[56] To this end, three dimensionless numbers, namely, the Euler number, the Weber number, and the capillary number, were used to assess the conditions leading to gas embolism. These numbers are defined as the ratio of inertial force to pressure force, the ratio of inertial force to interfacial tension, and the ratio of viscous force to interfacial tension, respectively (eqn (1)–(3)).[57]

$$\text{Euler Number} = \frac{\text{Pressure force}}{\text{Inertial force}} = \frac{\Delta P}{\rho_f \times {U_b}^2} \quad (1)$$

$$\text{Weber Number} = \frac{\text{Inertial force}}{\text{Interfacial tension}} = \frac{\rho_b \times {U_b}^2 \times d_H}{\sigma} \quad (2)$$

$$\text{Capillary Number} = \frac{\text{Viscous force}}{\text{Interfacial tension}} = \frac{\mu_l \times U_b}{\sigma} \quad (3)$$

where ρ_b is the density of the air bubbles in the channel (kg m^{-3}), ρ_f indicates the density of the fluid in the channel (kg m^{-3}), σ denotes the interfacial tension of the liquid and air bubble (N m^{-1}), d_H represents the hydraulic diameter of the channel (m), μ_l is the viscosity of the liquid (kg m^{-1} s^{-1}), U_b Indicates the bubble velocity (m s^{-1}), and eventually ΔP is the pressure drop (N m^{-2}).

3.2.4.a Impact of the inverse form of the Euler number on bubble–fluid flow dynamics

Inverse form of the Euler number versus channel width. Fig. 5A to F present the variation of the inverse form of the Euler number, *i.e.*, the ratio of the inertial force of the liquid to the pressure drop, for different air-to-liquid ratios. In conformity with the Hagen–Poiseuille relationship, larger channel widths translated in a pressure drop in the channel (Fig. 5A), overcoming the increase in fluid flow velocity, *i.e.*, 12, 42, and 90 μl h^{-1} for 20, 40, and 60 μm channels, respectively. Larger values of the inverse of the Euler number translated in a more seamless movement of the bubbles, as also shown in the initial observations on fluid flow resistances in narrow channels (Fig. S7, ESI†). Conversely, a lower value of the inverse Euler number suggests higher potential for gas embolism events.

Inverse form of the Euler number versus fluid viscosity. Depending on the Newtonian or non-Newtonian nature of the fluid, the inverse of the Euler number resulted in different relationships (Fig. 5C). However, an increase in the air-to-liquid ratios did not translate into faster bubble flow, as the increase in the air-to-liquid ratio did not increase the inverse form of the Euler number (or the ratio of inertial force to pressure force). This observation highlights the important effect of the viscous force *versus* other forces, underscoring its essential role as the primary counterforce against bubble motion and the primary force responsible for gas embolism events.

Inverse form of the Euler number versus junction type. The channels with 20 μm widths and T-junctions exhibited a consistent pattern of lower inverse Euler numbers and higher pressure drops compared to their counterparts with Y-junctions (Fig. 5). Starting from 40 μm widths, irrespective of the liquid viscosity, there was no noticeable difference between the values of the inverse Euler number between channels with T- and Y-junctions (Fig. 5B and D). The channels with 60 μm widths consistently presented a stratified flow pattern, regardless of the air-to-liquid ratio, except for ratios 10 and 20, when water (0% haematocrit equivalent) was used. Because of this stratified flow, under these specific conditions (Fig. 5B and D), it was not possible to calculate the Euler number (or its inverse form). The inverse Euler number for the 40 μm channels was higher than the 20 μm channels due to the higher importance of inertial force over the pressure force (Fig. 5B and D). This was also true for the flow with uniform bubbles when it came to the injection of the synthetic blood (Fig. 5E and F). The sudden alteration in fluid paths at the T-junction seems to play a crucial role in dissipating the energy linked to the movement of bubbles, resulting in a more significant drop in fluid pressure compared to the Y-junction channel.[58] Thus, a large pressure drop, the result of sharp joining angles, is one of the key factors contributing to the heightened risk of gas embolism. Though pressure drop due to inertial forces is a good first indicator for predicting the halting of bubble movement, a strong interplay exists involving other forces, namely, shear stress, viscous forces, and interfacial tension.

3.2.4.b Impact of the Weber number on bubble-stability and sizes. The Weber number, which is the ratio of inertial force, *i.e.*, the driving force responsible for bubble flow, to that of

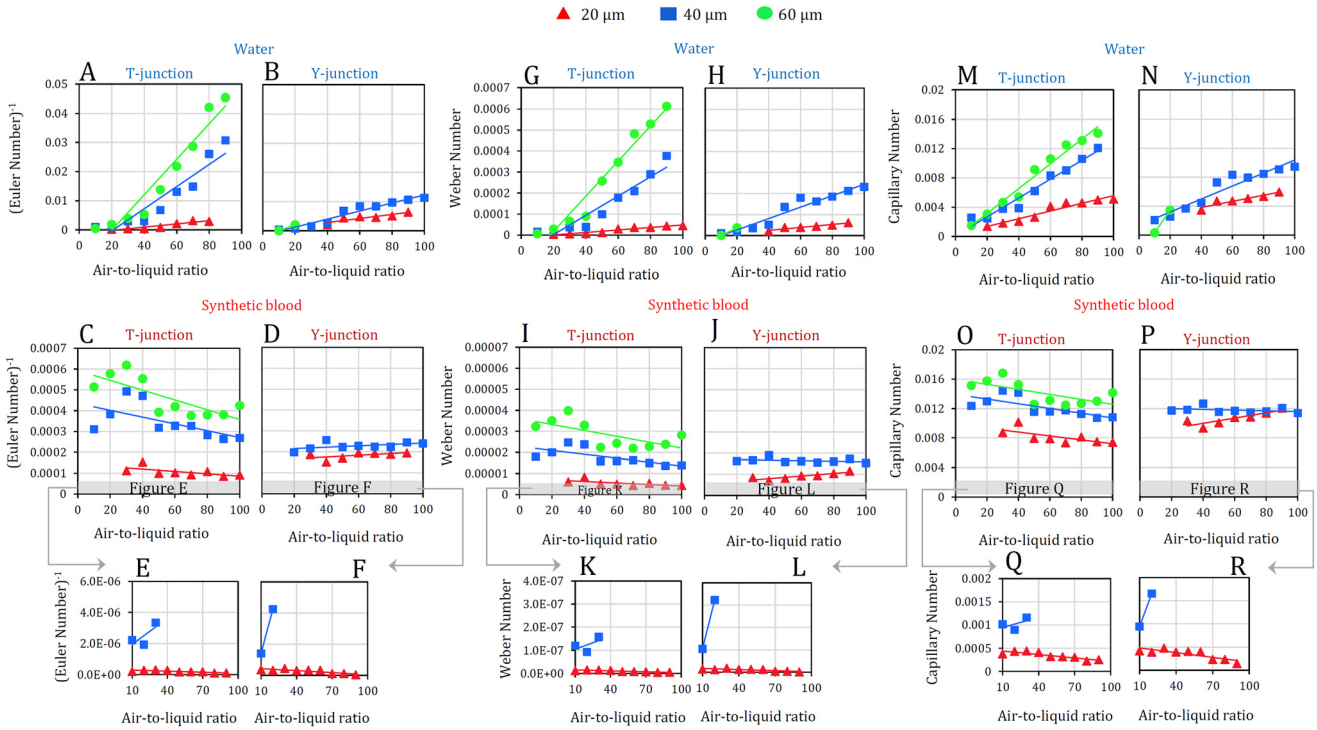

Fig. 5 The impact of junction type, channel width, air-to-liquid ratio, and liquid viscosity on the dimensionless numbers of the channels. The figures are divided into three categories: the inverse form of the Euler number is represented by (A)–(D) – where (A) and (B) correspond to water at T-junction and Y-junction channels, respectively, while (C) and (D) represent synthetic blood at T-junction and Y-junction channels respectively. The inverse form of the Euler number for the flow with uniform bubbles in synthetic blood at T-junction and Y-junction channels is depicted in Fig. 5E and F, respectively. The Weber number is denoted by (G)–(J) – with (G) and (H) showcasing water at T-junction and Y-junction channels, respectively. (I) and (J) represent synthetic blood at T-junction and Y-junction channels, respectively. The Weber number for the flow with uniform bubbles in synthetic blood at T and Y-junctions is depicted in Fig. 5K and L, respectively. Lastly, the capillary number is depicted by (M)–(P) – where (M) and (N) correspond to water at T-junction and Y-junction channels, respectively, and (O) and (P) represent synthetic blood at T-junction and Y-junction channels respectively. The capillary number for the flow with uniform bubbles in synthetic blood at T-junction and Y-junction channels is depicted in Fig. 5Q and R, respectively.

interfacial tension, *i.e.*, surface tension-derived resistance force to bubble flow, is another essential indicator of the possibility of channel blockage by bubbles. A low Weber number value indicates the prevalence of interfacial force over the inertial force of the bubbles in the channels and, therefore, an increased likelihood of the cessation of bubble movement and blockage of the flow. Also, the Weber number was used here as an indication of the stability of the bubbles.[59] For a higher Weber number, it will result in interfacial distortions, breakup, and merging of the air bubbles. Conversely, with low values of the Weber number, the bubbles will maintain their shapes and sizes, with minimal distortions during their passage through channels,[60] that is, an increased likelihood of gas embolism events.

Weber number versus channel width and viscosity. The variation of the Weber number as a function of channel widths, liquid viscosity, and different air-to-liquid ratios for the two junction types is presented in Fig. 5G to L. The relationship between the Weber number of the dispersed phase (in this case, air) and the volume of the bubbles presented a direct relationship, that is, higher Weber numbers correspond to larger bubble sizes. A comparison between Fig. 3 and Fig. 5G to L supports the validity of these findings, along with another study[50] showing that bubble sizes are directly proportional to the Weber number. Higher values of the Weber number, due to higher inertial force, were observed for larger channel widths (Fig. 5G to L), thus leading to a decreased likelihood of channel blockage, irrespective of the liquid viscosity and junction type. Importantly, as fluid viscosity increased, the values of the Weber number decreased by over 15-fold. This observation is significant, given that the interfacial tension of synthetic blood (approximately 49 dyne cm^{-1}) was lower than that of water (72 dyne cm^{-1}). Despite this, the marked reduction in the Weber number underscores the essential role of the inertial force of the bubble, which experiences a significant reduction as liquid viscosity increases. As depicted in Fig. 3E to H, it was evident that the velocity of the bubbles, a key factor predominantly affecting the inertial force of the bubbles, also reveals a strong dependence on the viscosity of the liquid.[61]

Weber number versus air-to-liquid ratio. An increase in the air-to-liquid ratio of the channel hosting water flow resulted in an increase in the Weber number. Since the interfacial tension of the liquid was constant, increasing the air flow rate increased the inertial force of the moving bubbles and consequently decreased their stability. For channels with 20

μm widths, no significant increase in the Weber number with an increase in the air-to-liquid ratio was observed (Fig. 5G and H). This observation extended to synthetic blood, irrespective of the channel widths and junction types. The flow with uniform bubbles was associated with the lowest Weber number (Fig. 5K and L), and consequently, the potential of the channel blockage in this situation was higher than in other cases (namely, the flow with uniform bubbles presented in Fig. 5G to J).

Weber number versus channel junction. Irrespective of the channel width and liquid viscosity, the Weber numbers in channels with Y-junctions were marginally higher than those in channels with T-junctions, indicating a slightly higher stability of the bubbles. In channels with 40 μm widths and with T-junctions, for high air-to-liquid ratios, the Weber numbers were higher than their corresponding values for the Y-junction channels. However, at the low and middle values of air-to-liquid ratios, the Weber numbers for Y-junction channels were higher than those for channels with T-junctions. Based on these results, the highest potential of the gas embolism events occurred for the flow with uniform bubbles in the channels with T-junctions (Fig. 5K).

3.2.4.c Impact of the capillary number on bubble–fluid flow dynamics. The effect of shear stress on the bubble dynamics manifests as four different regimes,[62] *i.e.*, the squeezing regime, dripping regime, jetting regime, and tip streaming, all of which are governed by the capillary number.[63] The squeezing regime typically leads to the formation of bubbles longer than the channel width (Fig. 2D), while the dripping regime yields smaller bubbles (Fig. 1B). In the jetting regime, the size of the bubbles is between those of the dripping and squeezing regimes (Fig. 2C). Tip streaming produces very small bubbles, considerably smaller than the channel size.[64] At low capillary numbers, *i.e.*, when surface tension forces are predominant, bubbles form in the squeezing regime. A gradual increase in the capillary number translated from the squeezing to the dripping regime and then from the dripping to the jetting regime at high capillary numbers. The formation of bubbles in a stratified parallel flow, observed mostly in Y-junction channels, was predominately influenced by the viscous force.[65] Based on the microscopy images of the evolution of bubbles and their size distributions, the squeezing, dripping, jetting, and stratified (or parallel) regimes were the only ones observed in this study, with the tip streaming regime not being detected.

Capillary number versus channel width, fluid viscosity, and air-to-liquid ratio. Fig. 5M to R present the variation of the capillary number with respect to the channel width, fluid viscosity, and air-to-liquid ratio. The lowest capillary number is associated with the flow with uniform bubbles. Based on the data presented in Fig. 5E and F, the smallest size of the bubbles was observed for the flow with uniform bubbles, which had the lowest velocity compared to the other flow patterns (Fig. 3G and H). The transition from the flow with uniform bubbles to the flow with non-uniform bubbles increased the capillary number noticeably (Fig. 5M to R). This transition occurred when the number of uniform bubbles increased significantly, translating into a decreased distance between two adjacent bubbles. A gradual decrease in this distance brought about the frequent coalescence of adjacent bubbles extending along the channel. The motion of the uniform bubbles in the form of a squeezing regime occurred when the capillary number was lower than 0.002.

Capillary number versus bubble stability. Low values of the capillary number are the result of the prevalence of the interfacial tension over the viscous forces, translating into stable and persistent bubbles.[55] The bubbles produced during the motion of uniform bubbles (Fig. 5Q and R) had the highest stability compared to the flows with non-uniform bubbles presented in Fig. 5M to P. Higher capillary numbers were observed in larger channels, leading to a decrease in the stability of the bubbles. For instance, the bubbles flowing in channels with 20 μm widths presented the highest stability, irrespective of the liquid viscosity and air-to-liquid ratios. For water, an increase in the air-to-liquid ratio resulted in an increase in the capillary number and, thus, a decrease in the stability of the bubbles (Fig. 5M and N). As a result, for water, when the air-to-liquid ratio is high, the bubbles tend to break up more easily compared to situations with low ratios.

An increase in the fluid viscosity translated to an increase in the capillary number (Fig. 5O and P). At low air-to-liquid ratios, *i.e.*, between 10 and 30, the magnitude of capillary numbers for synthetic blood was higher than their corresponding values for water. Furthermore, variations in liquid viscosity did not yield significant changes in the capillary numbers for different air-to-liquid ratios. This observation suggests that even for a high injection rate of air, the prevailing influence of viscous forces over interfacial tension remains unaffected. As a result, the stability of injected air bubbles would not be compromised.

3.3 Mapping high-risk regimes for the incidence of gas embolism using dimensionless numbers

The dimensionless analysis presented above was used to assess the high-risk conditions leading to gas embolisms, such as channel width, viscosity, and liquid-to-air flow ratios, presented in 3D bubble charts (Fig. 6). The relation between two different dimensionless numbers, namely, Weber and capillary numbers was used to predict bubble halting, and bubble collapsing in the channels across different air-to-liquid ratios. In the context of physiological relevance, bubble halting may trigger the blocking of the flow in the microvasculature, and then, subsequently, biochemical and physiological inflammatory responses, such as the formation of thin films on the bubble surfaces, white clot formation, and, eventually, the red blood clot.[66] In contrast, bubble collapse may trigger the easing of the gas embolism severeness in some locations, but it may also trigger the blocking of blood flow in narrower vessels. For particular operational conditions, *i.e.*, viscosity and air-to-liquid ratio, the size of the bubble was inversely proportional to the total number of the bubbles. In channels with T- and

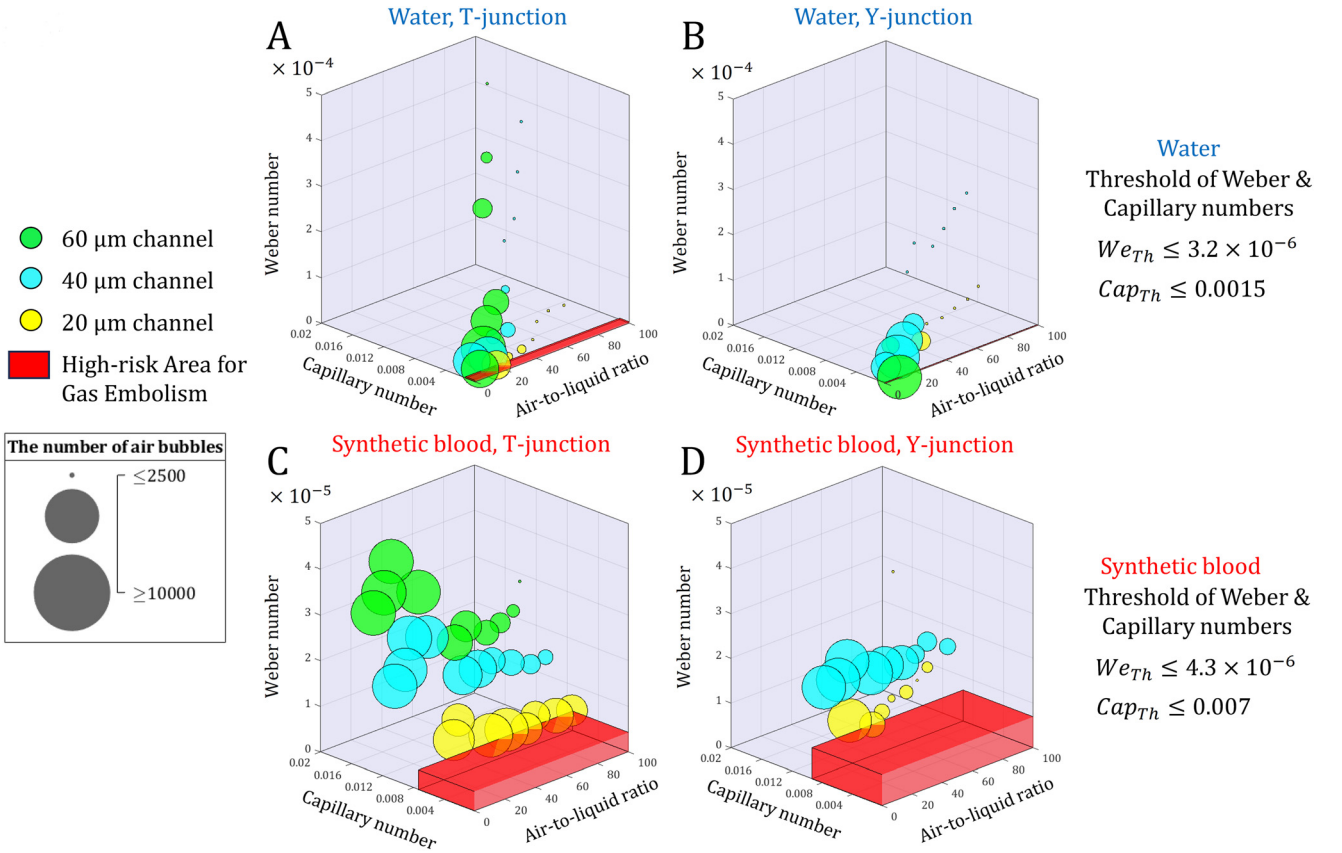

Fig. 6 Bubble charts illustrating Weber and capillary number variations for different air-to-liquid ratios. (A) Water in a T-junction channel, (B) synthetic blood in a T-junction channel, (C) water in a Y-junction channel, and (D) synthetic blood in a Y-junction channel. The elevation of each bubble corresponds to the order of Weber numbers, and the size of the bubbles represents the number of bubbles. The smallest bubble denotes a minimum of 2500 bubbles, while the largest one indicates a minimum of 10 000 bubbles. The red zone, designating the high-risk region for gas embolism occurrence, was established based on the minimum values of the Weber and capillary numbers. These specific threshold values, which mark the areas with the highest risk for gas embolism incidence and bubble cessation, were documented on the right side of the charts.

Y-junctions carrying water, an increase in the air-to-liquid ratio resulted in a smaller number of bubbles (Fig. 6A and B). This observation correlates with the findings in Fig. 3A to D, where an increase in air-to-liquid ratio leads to longer bubbles and, consequently the reduction of the number of bubbles in the channel. An increase in liquid viscosity resulted in an increase of the number of bubbles and a reduction of the length of the bubbles (Fig. 6C and D). Finally, the type of channel junction modulated the number of bubbles. For instance, at the same viscosity and air-to-liquid flow ratios, channels with T-junctions had more moving bubbles than those with Y-junctions.

The high-risk area for gas embolism, based on bubble lengths and total bubble counts, was categorized based on the threshold regions, *i.e.*, minimum values of the Weber number (representing the centre of the bubble at the lowest elevation) and the minimum value of the capillary number marked as red regions (right side of the charts in Fig. 6C and D). For example, when considering synthetic blood inside the channels with T-junctions, the high-risk area is surrounded by a regime with a large number of bubbles flowing through 20 μm channels for all air-to-liquid ratios. As depicted in Fig. 6C, both the quantity of air bubbles and the threshold values of Weber and capillary numbers suggest that channels with T-junctions and high-viscosity liquids present a higher risk of gas embolism. However, the role of viscosity in increasing the likelihood of gas embolism was more significant than the impact of the junction type. For instance, the yellow circles predominantly falling in the red region for Fig. 6C (representing the same conditions for T-junctions) moved away from the red region in Fig. 6D, for the Y-junction, except for low air-to-liquid flow ratios, *i.e.*, up to 1 : 40.

3.4 Quantitative prediction of dimensionless numbers in wider channel widths

The dataset of dimensionless numbers for various air-to-liquid ratios and channel widths allowed the development of a function assessing the potential for gas embolism occurrence in channels with wider widths than those experimentally tested here. This function correlates all relevant dimensionless numbers, namely Weber, capillary, and the inverse form of Euler numbers. These dimensionless numbers were the dependent variable to two independent variables, namely the air-to-liquid ratio and channel width. It was found that a fourth-order polynomial function correlates well with experimental data:

$$\text{Dimensionless Number} = C_4R^4 + C_3R^3 + C_2R^2 + C_1R + C_0 \quad (4)$$

$$C_i = A_{j1}d_H + A_{j0} \quad (5)$$

where R is the air-to-liquid ratio, and C_i (*i.e.*, C_4, C_3, C_2, C_1, and C_0) are the coefficients of the polynomial function. C_i is a linear function of the hydraulic diameter. The coefficients of this linear function are denoted as A_{j1} and A_{j0}. All coefficients, together with the respective correlation coefficients, are presented in Table S4 in the ESI.†

Fig. 6 illustrates the variations in dimensionless numbers modulated by different values of channel width from 20 to 2000 μm for all air-to-liquid ratios. The regression analysis demonstrated a strong correlation between the fitted curve and experimental data (inset Fig. 7). By employing the specified function and considering the air-to-liquid ratio, the dimensionless number corresponding to the desired channel width can be predicted. This calculated dimensionless number subsequently facilitates the determination of bubble velocity, incorporating essential blood properties, including density, viscosity, and interfacial tension. The velocity of the bubble serves as an indicative parameter for predicting the distance it covers within a specified time frame. Moreover, the magnitude of the velocity serves as an estimator for its potential to come to a stop, *i.e.*, the potential for a gas embolism event.

3.5 Complex honeycombed network

The processes mimicking gas embolism *in vitro* were also studied in uniform bifurcation 'honeycombed' microfluidic networks. These networks comprised 30 μm wide, Y-junction inlets and five levels of bifurcating channels (Fig. 1B). From the results in channels with T- and Y-junctions, it can be inferred that the flow in 60 μm channels had a monotonous stratified flow during the continuous inlet of air in a liquid flow regime. Consequently, channels with 30 μm widths were chosen for all experiments using bifurcation networks. The main objectives of using honeycomb networks for studying gas bubble and liquid slug behaviour were to explore if any angles in microchannels would preferentially induce gas bubble trapping, especially in bifurcations, as well as if the air bubbles are washed, or broken-up, at high air-to-liquid ratios. Furthermore, the experiments with honeycomb

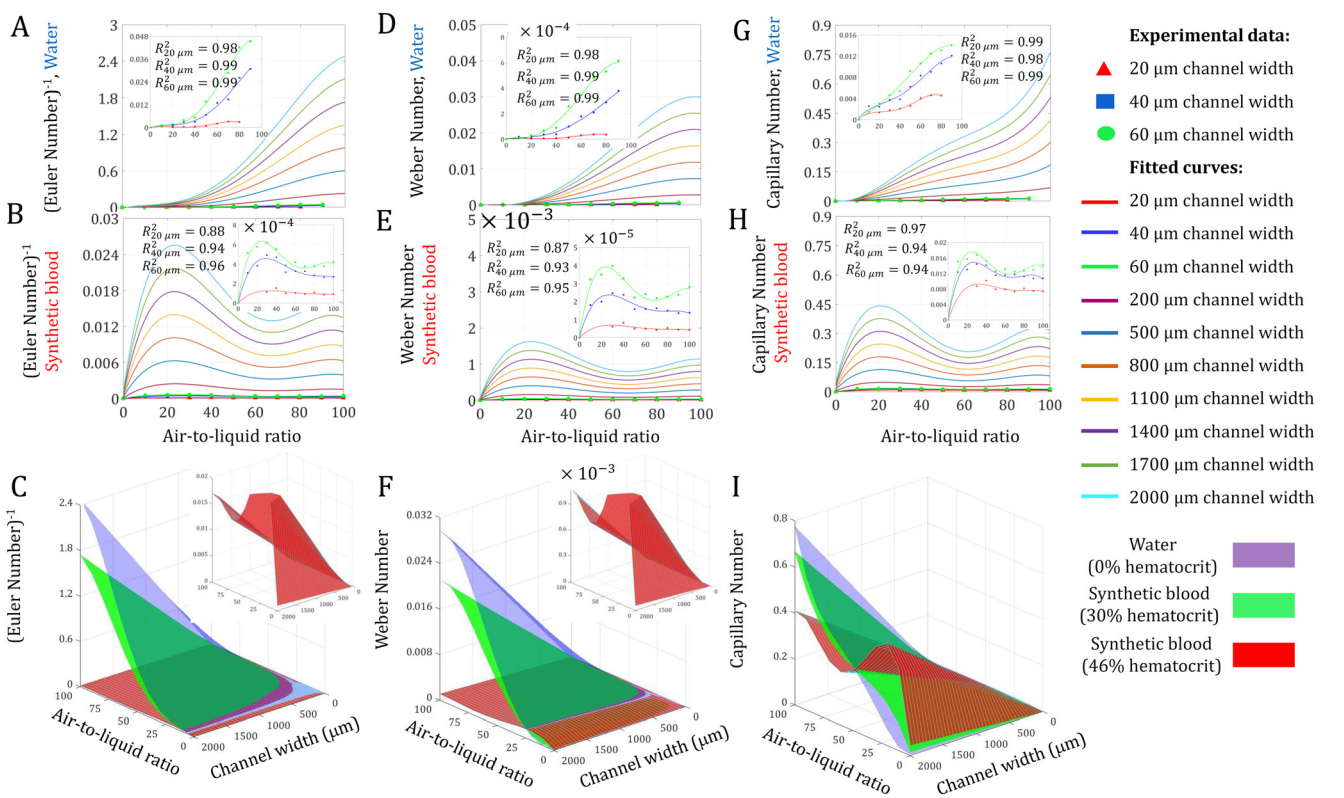

Fig. 7 The estimation of dimensionless numbers in larger T-junction channels based on the fourth order polynomial function to predict the potential of gas embolism. Inverse form of the Euler number of (A) water, (B) synthetic blood (46% haematocrit) and (C) water and synthetic blood with haematocrit percentages of 30 and 46%; the Weber number of (D) water, (E) synthetic blood (46% haematocrit) and (F) water and synthetic blood with haematocrit percentages of 30 and 46%; and the capillary number of (G) water and (H) synthetic blood (46% haematocrit) and (I) water and synthetic blood with haematocrit percentages of 30 and 46%. The regression analysis demonstrated a strong correlation between the fitted curve and experimental data (inset figures). Through this function, the estimated values of dimensionless numbers for different channel widths can be obtained. With these estimates and considering the properties of the fluid (such as density, viscosity, and interfacial tension), it becomes possible to predict the bubble velocity within that specific channel width. This capability is of great importance from a medical perspective, as it aids in assessing the potential incidence of gas embolism.

geometries focused on assessing the impact of the bifurcation angle on the bubble size, bubble flow, traffic density in the channels (Laplace displacement of bubbles in complex geometries) and time-resolved flow dynamics. Also, the angles of bifurcation, *i.e.*, 30°, 45°, and 60°, chosen for this study, were similar to those commonly observed in mammals, *e.g.*, pigs and humans.[67,68] A qualitative analysis of the traffic density of bubbles and active dynamic regions of fluid flow of the honeycomb network is presented in Fig. 8A and ESI† Movie S3.

Mapping dynamic locations of bubbles in the network. The density maps correspond to the most visited routes in the bifurcation network for air bubbles and liquid slugs. The density maps were derived as total sums of the positions of air bubbles and liquid slugs in all the frames recorded for different air-to-liquid flow ratios and equivalent concentrations of haematocrit. The dark regions correspond to blocked channels in the network, while regions with various intensities of blue to yellow correspond to the propensity of the respective path being visited by the flow of liquid slugs and air bubbles. The bifurcation network showed three prominent flow patterns (Fig. 8A): (i) flow in a single channel, (ii) flow in part of the networks, and (iii) flow in the entire network.

The flow of liquid slugs and air bubbles along a single path (Fig. 8A, first three columns) was observed for all the tested bifurcation angles for an air-to-liquid ratio ranging from 10 up to 40. For air-to-liquid ratios higher than 60 in honeycomb networks with 90° bifurcation angles, no prominent flow paths were observed. The density maps indicate that for 60° bifurcation angles, there is an effective flow path of air bubbles and liquid slugs, whereas for 90° bifurcation angles, there is a higher propensity for blockages, especially at higher air-to-liquid ratios. In regions with little or no traffic of air bubbles, the liquid slug movement was often blocked, similar to gas embolism-like behaviour, which occurred preferentially at the periphery of the honeycomb network. In contrast, networks with 30° bifurcation angles induced a flow pattern across the entire network.[28]

Mapping stagnant features and blockages in the network. A median analysis of the image pixels for measuring the stagnant regions of the network was performed. The median analysis demarcates the regions with entrapped bubbles (no traffic of the fluids) from continuous total slug flow (fluid flow traffic), revealing the blockages (Fig. 8B) due to trapped air bubbles and the stagnant regions of the network. In Fig. 8B, the prevalence of gas bubbles and blockages at 40 air-to-liquid flow ratios in 60° and 90° bifurcations is

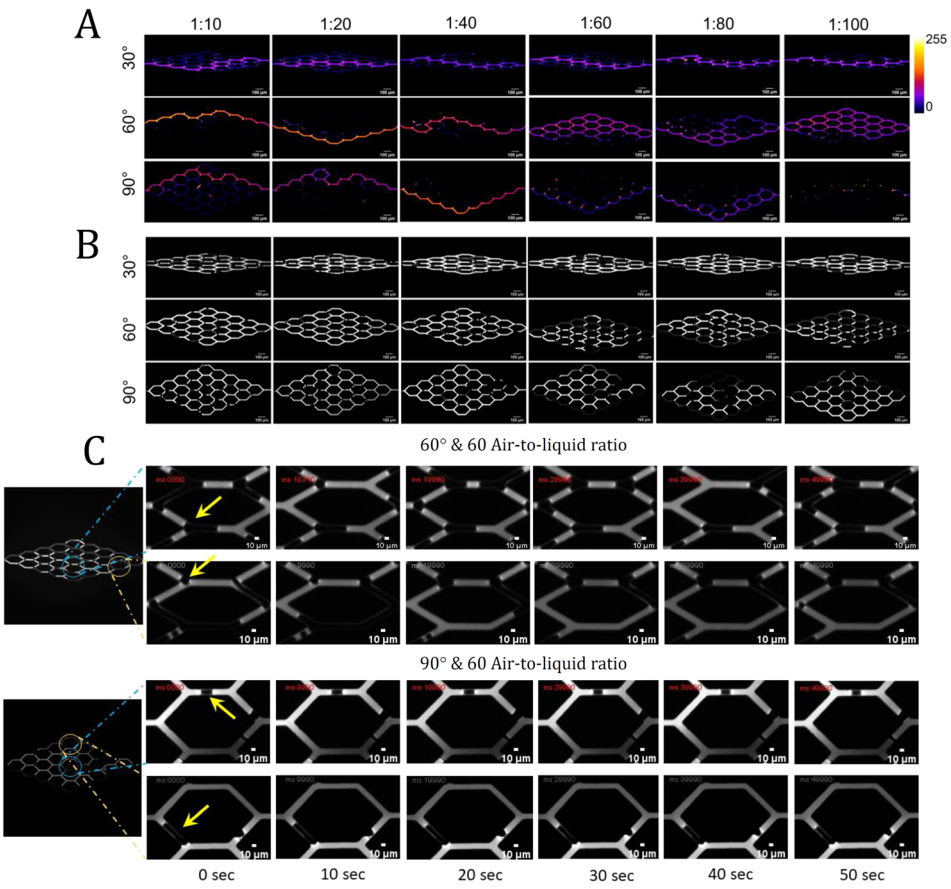

Fig. 8 (A) The total traffic density of the liquid slug is bubble traffic in a complex bifurcation network for three different bifurcation angles. Higher intensities represent higher liquid slug to air bubble traffic. The dark channels represent blocked paths. (B) Median pixel intensity plots of the blocked channels and traffic patterns for three differently angled bifurcations. (C) Time-resolved image analysis of the resilient bubbles.

remarkable. The bifurcation channels with 60° angles present gas emboli blocking selective regions of the network (bubble blocking the channels is shown as dark regions). The dark or less-illuminated areas represent channels where continuous fluid flow did not occur due to blockages by gas bubbles.

Impact of bifurcation angles and air-to-liquid ratios on bubble parameters. Comparing the characteristics of fluid flow in networks with the smallest bifurcation angles, *i.e.*, 30°, and low air-to-liquid ratios, *i.e.*, less than 60, the total slug, *i.e.*, namely liquid slug and air bubble, followed a single path in the network, rather than multiple ones. Conversely, at higher air-to-liquid ratios, *e.g.*, above 80, the liquid dominated the flow in channels of the entire network with a mixture of liquid slugs and varying lengths of air bubbles. The median analysis showed that acute bifurcation angles increased blockage probability. In Fig. 8C, the statistics were plotted from different track measurements (n = 20) for different conditions, like bifurcation angles and air-to-liquid ratios. The prevalence of gas bubbles and blockages at 60 air-to-liquid flow ratios in 60° and 90° bifurcations was observed. In the bifurcation channels with 60-degree angles, gas emboli were observed to block at the junctions, while those with 90-degree bifurcation angles exhibited the formation of emboli. Yellow arrows indicate the position of the bubble stagnant over a period of time. The position of the bubble was predominant across each row of the images.

Bubble flow and entrapment patterns. Three types of network blockages were observed, as shown in the timelapse of the positions of air bubbles (Fig. 8C): (i) blockages at the bifurcation junctions, (ii) blockages in the channels, and (iii) blockages at both bifurcation junctions and in the channels. Representative bifurcations with blocked bubbles at different time points are presented in Fig. 8C. During high-speed imaging, the stagnant points seldom lasted longer than 50 seconds. Also, by analysing the images collected at 100 fps for over 1 minute, *i.e.*, approx. 6000 frames, and inspecting the movement patterns of the air bubbles and liquid slugs in the network, the following conclusions were drawn:

(i) Regardless of the rate of air-to-liquid ratio, the incoming bubbles from the inlets moved preferentially along the paths without bubble obstruction. As the air bubbles traversed the bifurcations and continuously entered the nodes without air bubbles, they eventually blocked all possible routes, which led to the blockage of some regions in the network with no liquid flow (ESI,† Movie S3). This process was observed across a wide range of flow rates (10 to 100) for all bifurcation angles but more often for 90° and 60° angles.

(ii) The bifurcations towards the middle of the honeycomb network induced more air blockages (Fig. 8) compared with earlier ones. This is to be expected as the air bubbles at the entry start to branch out, leading to air bubbles crowding in the second half of the network, resulting in blockages across the converging channels of the network.

(iii) The processes mentioned above at points (i) and (ii) led to partial blocking of many nodes. At moderate air-to-liquid ratios, *i.e.*, between 20 and 60, the blocking effect was prominent for 30° and 60° angles. The networks with 90° bifurcation angles presented the most frequent air bubble trapping, followed by 60° bifurcations at air-to-liquid ratios above 60. A characteristic outcome of gas embolism in tissues is the reduced blood supply and oxygen transport to parts of the tissue, known as tissue ischemia. Tissue ischemia results in the blocking of vital nodes and junctions of the blood vessels to any tissue type in the body, such as cardiac, cerebral, *etc.* The present observation of selective multiple node blockages and gas entrapment is similar to the medical condition.[69]

(iv) Monitoring the motion of bubbles in honeycomb networks demonstrated that they move in the entirety of the network with acute angles, *e.g.*, 30°. Conversely, in networks with 60° bifurcation angles, partial regions were blocked due to trapped bubbles over for a longer period (more than 1 minute). In networks blocked with air bubbles, *i.e.*, 60° and 90° bifurcations, the flow remained obstructed until the flow rate was increased, leading to the distribution of the incoming air mixtures. The unpredictable nature of the flow in networks can be attributed to the unpredictability of the localized pressure drops in channels.

The architecture in the honeycomb structure is analogous to capillary networks in tissues and the lungs,[70,71] whereas branching inlets are analogous to the venous system.[72] The branching of arterial vessels reaches the heart and the far-end regions of the heart tissues.[73]

3.6 Biomedical relevance of this *in vitro* study to gas embolism-like events

While the environment surrounding air bubbles was previously studied,[74] our work, which focused on the physical parameters of air bubbles and liquid slugs inside channels, prompted some medically relevant findings.

The air-to-liquid ratio. Previous work[75] reported that the direct introduction of air into human tissues, with volumes ranging from 300 to 500 ml (equivalent to 2–5 ml kg^{-1}), carries a significant risk of fatality, with lethality being reached for an air injection rate of 100 ml s^{-1}. Taking into consideration these critical thresholds and accounting for the volume of blood present in individual organs relative to their respective weights, Table 1 provides estimated values for the likely fatal volume of air and the corresponding fatal air-to-blood ratio in the context of surgical procedures leading to iatrogenic gas embolism. Using the established fatal air-to-liquid ratio, it is possible to derive threshold values for capillary, Weber, and the inverse form of Euler numbers for each channel width, as presented in Fig. 5. Performing invasive medical procedures in conditions far from these critical ratios and operating within safety margins appears to be essential for avoiding gas embolism scenarios. It is important to stress that on the one hand, *in vivo* investigations are essential to validate these predictive findings, but on the other hand these estimated thresholds help optimize future experimental efforts.

Table 1 Relationship between the microfluidic chip design and properties of working fluids on gas embolism-relevant parameters

Organ	Blood volume (ml)[97]	Organ weight (g)[98–100]	Blood flow rate (ml min^{-1})	Fatal volume of air (ml)	Fatal gas-to-blood ratio	Surgical procedures prone to iatrogenic gas embolism
Brain	111	1336	672	2.7–6.7	8.9	• Craniotomy[101] • Cerebral angiography[102] • Neuroendoscopy[103]
Heart	124	316	224	0.6–1.6	26.8	• Transaortic valve replacement[104] • Pericardiocentesis[105]
Lungs	566	1000	140	2–5	42.9	• Thoracoscopy[106] • Percutaneous lung biopsy[107] • Bronchoscopy[108] • Lobectomy[109] • Thoracotomy[110] • Pleurodesis[111] • Pneumonectomy[112]
Major blood vessels	4130[a]	4130	3920[a]	8.3–20.7	1.5	• Thoracic endovascular aortic repair[113] • Central venous catheterization[114] • Coronary artery bypass grafting[115] • Coronary angiography[116] • Cardiopulmonary bypass[117]
Kidneys	70	229	1064	0.5–1.1	5.6	• Nephrectomy[118] • Hemodialysis[119] • Percutaneous Nephrolithotomy[120]
Liver	230	1910	364	3.8–9.6	16.5	• Hepatectomy[121] • Endoscopic cholangiopancreatography[122] • Laparoscopic cholecystectomy[8]
Gut	194	1200	840	2.4–6	7.1	• Gastrointestinal laparoscopy[123] • Gastrointestinal endoscopy[17] • Laparoscopic sleeve gastrectomy[124]
Bone	557	6120	280	12.2–30.6	21.4	• Arthroplasty[125] • Vertebroplasty[126] • Kyphoplasty[127] • Discectomy[128]

[a] 70% of total blood volume and 70% of total cardiac output were considered for the major blood vessels, respectively.[129]

The dynamics of gas embolism. Aside from the accidental or intentional introduction of air in blood flow, and while the medical causes are extremely varied, the phenomenological basis of *in situ* gas embolism is always the same, that is, instantaneous[76] and sudden decrease of the pressure surrounding blood reverses gas absorption, with dissolved gas transferring back to the gaseous phase, thus generating emboli.[77] The genesis of emboli is near-instantaneous, but various elements present in blood, such as proteins, lipids, and cells, form a membrane at the gas/blood interface, slowing gas dissolution back into the blood.[78] The fact that, at least at its inception, gas embolism is a purely physical process offers an opportunity, possibly nearly unique, to study it *in vitro* and *ex situ* in microfluidic networks mimicking microvasculature and the relevant preconditions. While the understanding of the initial stages of gas embolism can lead to medical guidance for the immediate intervention, microfluidics mimicking microvasculature can also help the calibration of hyperbaric treatment, which must continue until there is certainty that the patient has reached a steady state of medical plateau. While gas embolism can occlude blood flow, studies showed[79,80] that after injection of air into a vessel, a sizeable amount of gas passes into the venous circulation, possibly through diffusion into the nearby tissues, then back into blood behind the blockage of blood flow.[79,81]

T- and Y-junctions in the human body. Most blood vessels bifurcate in a Y-junction pattern.[82] Still, important T-junction exceptions occur, such as coronary arteries and Adamkiewicz arteries, an important supply artery to the spinal cord, which takes a "hairpin turn".[83,84] The central nervous system presents critical watershed areas with little collateral blood supplies. Future studies building on the methods described here could be valuable for elucidating mechanisms relevant to clinical gas embolism, as *in vivo* experiments are difficult and untenable due to their life-threatening features. Additionally, laminar flow increases the chances of iatrogenic air injection into the vessels, leading to rapid systemic embolism. The location of bubbles studied using the honeycombed device provided clues regarding the propensity of gas embolism in capillary and arterial-like bifurcation geometries.

Relevance of the studied channel width to physiological conditions leading to gas embolism. Most of the works using PDMS-based microvasculature for studying the behaviour of gas bubbles considered larger widths of the artificial blood vessels, that is, hundreds of micrometres. Conversely, due to the increasing reports on the prevalence of gas embolism and unpredictable bubble behaviour in channels of smaller

diameter,[28,85] this work considered channels with sub-100 μm widths. Also, bubble halting in the smallest vessels has been shown to lead to the most serious endothelial cells damage.[86] Further, it has been documented medically[28,85,87] that cerebral gas embolism intensifies in the smaller arteries of diameter ranging between 30 and 60 μm. Also, experimental evidence in mice and rat models has shown in multiple studies that gas bubbles in arterioles and venules, sub-100 μm channel widths, without verifiable blockage of the blood vessel, can have significant neurological deficits.[80,88–90]

Relevance of haematocrit equivalence and flow patterns to human haematocrit concentration. The impact of gas embolism may be influenced by blood viscosity,[53,91] high or low blood pressure, obesity, lipid and cholesterol levels, and medications such as anticoagulants ("blood thinners", *e.g.*, warfarin, aspirin).[92] Haematocrit percentages vary largely among men and women by 42.4% ± 2.9% and 47.2% ± 2.4%, respectively.[93] Also, the haematocrit concentration is generally less than 42% for anaemic individuals, although the concentration could be even lower depending on age and some medical conditions. Furthermore, haematocrit concentrations can also vary between the upper and lower body, *e.g.*, 40% ± 0.8% and 38.5% ± 0.8%, respectively. Therefore, the two different fluids studied here, *i.e.*, an equivalent of 0% and 46% haematocrit concentrations, are relevant to specific medical circumstances and conditions. Another example with possible medical relevance is for a haematocrit concentration of up to 46%, which is found in normal humans,[94] and an equivalent concentration of 0% haematocrit when using water-like solutions for irrigating internal organs when concluding surgery. Additionally, blood components like albumin can contribute to cell-free blood, which shares commonality with waterlike viscosity properties. Overall, the physical measurements of liquid slug behaviour presented here for different equivalent concentrations of haematocrit, including water as the reference liquid, are similar to the real blood-like or blood-similar fluids, thus making the presented study relevant to biological conditions.

Table 2 Relationship between the microfluidic chip design and properties of working fluids on gas embolism-relevant parameters

Chip design		Liquid	Liquid flow rate [μl h^{-1}]	Air flow rate [μl h^{-1}]	Key physical parameters and gas embolism-relevant outcome
T-junctions	20 40 60	Water and synthetic blood equivalent to 46% haematocrit	12 42 90	12–1200 42–4200 90–9000	Key physical observations • Higher liquid viscosity led to shorter and slower-moving bubbles • The slowest bubble velocity occurred in the 20 μm channel width • The 20 μm channel width had the highest potential for channel blockage for various force ratios • Increased liquid viscosity had the most significant impact on channel blockage, regardless of air-to-liquid ratio, when considering the Weber number • For the capillary number, bubbles introduced into the 20 μm channel exhibited the greatest stability Gas embolism relevance Smaller channel widths have higher chances of bubble trapping compared to larger channels. Some T junctions occur in critical and vulnerable tissues
Y-junctions	20 40 60	Water and synthetic blood	12 42 90	12–1200 42–4200 90–9000	Key physical observations • Higher haematocrit concentrations led to more alternating liquid slug and gas bubble flow • Increased haematocrit concentrations resulted in shorter and stable air bubbles, especially when compared to T-junctions with the same haematocrit equivalent • In 60 μm channel width, stratified flow was consistently observed, regardless of haematocrit concentration or air-to-liquid ratio Gas embolism relevance Y-junction is the least studied but the most abundantly found in animal vasculature.
Honeycombs	30° 60° 90°	Synthetic blood equivalent to 46% haematocrit	24	24–2400	Key physical observations • A 30° bifurcation angle translated in a higher occurrence of bubble trapping at less than 40 air-to-liquid flow ratios • At higher than 60 air-to-liquid flow ratios, 60° bifurcation angles showed the highest occurrence of flow blockage, *i.e.*, gas embolism-like events • The flows of liquid slugs and air bubbles were evenly distributed over the bifurcation network, translating into a lower propensity of gas embolism Gas embolism relevance The bifurcation angle is critical for bubble displacement and modulates the propensity of gas embolism events. Arterial-type bifurcations showed localized "tissue ischemia" blocking of traffic at partial locations in the network. Honeycomb structures exist at the sites of gas exchange in the body, *e.g.*, lungs and tissues

Table 2 summarizes the key findings from this study. The medical relevance of the different parameters considered, such as the different junction types, fluid flow and bubble dynamics using *in vitro* microfluidic approaches, is provided.

A potential way forward for studying, understanding, and potentially preventing gas embolism is to focus on the medical conditions involving parameters modulating hydraulic resistance, *i.e.*, flow rate, length, diameter, and wall properties of the blood vessels. Alternatively, various therapeutic medications can impact the hydraulic resistance within blood vessels and the characteristics of their walls. For instance, antihypertensive drugs and vasodilators can help relax and widen blood vessels, thereby reducing resistance to blood flow. Anticoagulants may affect the properties of the blood vessel walls, and antiplatelet agents can reduce the stickiness of platelets, potentially affecting interactions with blood vessel walls. Furthermore, investigating advanced surgical approaches, including microsurgical anastomosis techniques[95] or the utilization of microrobots[96] for adjusting blood vessel length and diameter in regions with an elevated risk of bubble entrapment, presents potential research directions for the future.

4 Conclusions

Depending on geometrical variations and operational parameters, air bubble dynamics and liquid slug flows were monitored in simple linear channels and more complex honeycomb structures. The present work analysed smaller channel widths and liquid flow rates relevant to actual physiological conditions and used fluids close to real blood viscosities derived from different haematocrit concentrations. Microvascular tissue-like structures using microfluidic networks with T- and Y-junctions and honeycombed networks were used, in line with their biological relevance. The study revealed correlations between input variables of gas embolism, *i.e.*, fluid viscosity, equivalent concentrations of haematocrit, air-to-liquid ratio, and channel widths on output variables, *i.e.*, air bubble and liquid slug lengths and velocities, thus offering insights into the fundamentals of this devastating medical condition. Research on transport phenomena, gas embolism in microvasculature with smaller widths and more complex bifurcations with real blood, and other conditions, *e.g.*, clot formation, will be relevant subjects of future studies.

Data and materials availability

All data is available in the main text or ESI.†

Author contributions

Mohammad Mahdi Mardanpour: conceptualization, methodology, validation, formal analysis, investigation, image analysis, writing (original draft, review and editing), visualization. Ayyappasamy Sudalaiyadum Perumal: conceptualization, methodology, validation, formal analysis, investigation, writing (original draft, review and editing), visualization. Zahra Mahmoodi: image analysis. Karine Baassiri: image analysis. Gala Montiel Rubies: image analysis, writing (review and editing). Kenneth M. LeDez: medical interpretation of results, writing (review and editing). Dan V. Nicolau: conceptualization, methodology, validation, formal analysis, review and editing of the original draft, visualization, supervision, project administration, funding acquisition.

Conflicts of interest

The authors declare no competing interests.

Acknowledgements

Research supported by the Canadian Natural Sciences and Engineering Research Council (NSERC) grant no. RGPIN-2016-05019. We thank the research personnel from Nano-UQAM, especially Dr. Galyna Shul, for their help with photolithography and microfabrication.

Notes and references

1 S. Goldman, J. M. Solano-Altamirano and K. M. Ledez, in *Gas Bubble Dynamics in the Human Body*, ed. S. Goldman, J. M. Solano-Altamirano and K. M. Ledez, Academic Press, 2018, pp. 1–48, DOI: **10.1016/B978-0-12-810519-1.00001-4**.
2 G. Cueto-Robledo, E. Roldan-Valadez, A.-C. Mendoza-Lopez, P. Palacios-Moguel, A.-L. Heredia-Arroyo, I.-D. Torres-Lopez, M. Garcia-Cesar and M.-B. Torres-Rojas, *Curr. Probl. Cardiol.*, 2022, 101248.
3 K. M. LeDez, *Can. J. Anaesth.*, 2011, **58**, 1140–1141.
4 C. J. McCarthy, S. Behravesh, S. G. Naidu and R. Oklu, *Diagnostics*, 2017, **7**, 5.
5 A. Verma and M. P. Singh, *J. Anaesthesiol., Clin. Pharmacol.*, 2018, **34**, 103.
6 P. Mandelstam, C. Sugawa, S. E. Silvis, O. T. Nebel and G. Rogers, *Gastrointest. Endosc.*, 1976, **23**, 16–19.
7 A. B. Branger and D. M. Eckmann, *J. Appl. Physiol.*, 1999, **87**, 1287–1295.
8 K. I. de Jong and P. W. de Leeuw, *Eur. J. Intern. Med.*, 2019, **60**, 9–12.
9 S. Allioui, S. Zaimi, S. Sninate and M. Abdellaoui, *Radiol. Case Rep.*, 2020, **15**, 1011–1013.
10 C. Yang and B. Yang, *Neuroradiology*, 2005, **47**, 892–894.
11 J. Klein, T. A. Juratli, M. Weise and G. Schackert, *World Neurosurg.*, 2018, **115**, 196–200.
12 T. Wu, Q. Wang, M. Zhao, Y. Zhu, L. Zhang, Y. Li and J. Li, *J. Forensic Leg. Med.*, 2021, **82**, 102209.
13 P. Brandner, K. J. Neis and C. Ehmer, *The Journal of the American Association of Gynecologic Laparoscopists*, 1999, **6**, 421–428.
14 S. Q. Liu, S. Z. Zhao, Z. W. Li, S. P. Lv, Y. Q. Liu and Y. Li, *J. Med. Ultrasound*, 2017, **36**, 749–756.
15 V. Arena and A. Capelli, *Cardiovasc. Pathol.*, 2010, **19**, e43–e44.

16 N. Shaikh and F. Ummunisa, *J. Emerg. Trauma Shock*, 2009, **2**, 180.
17 S. Donepudi, D. Chavalitdhamrong, L. Pu and P. V. Draganov, *World J. Gastrointest. Endosc.*, 2013, **5**, 359.
18 L. Riddick and B. G. Brogdon, *Am. J. Forensic Med. Pathol.*, 2012, **33**, 110–112.
19 P. Zou, J.-S. Yang, X.-F. Wang, J.-M. Wei, H. Guo, B. Zhang, F. Zhang, L. Chu, D.-J. Hao and Y.-T. Zhao, *World Neurosurg.*, 2020, **138**, 201–204.
20 T. S. Neuman, *Physiology*, 2002, **17**, 77–81.
21 A. M.-H. Ho and E. Ling, *The Journal of the American Society of Anesthesiologists*, 1999, **90**, 564–575.
22 S. J. Brull and R. C. Prielipp, *J. Crit. Care*, 2017, **42**, 255–263.
23 C. Ross, R. Kumar, M.-C. Pelland-Marcotte, S. Mehta, M. E. Kleinman, R. R. Thiagarajan, M. B. Ghbeis, C. J. VanderPluym, K. G. Friedman and D. Porras, *Chest*, 2021, 791–802.
24 M. Ljubkovic, J. Marinovic, A. Obad, T. Breskovic, S. E. Gaustad and Z. Dujic, *J. Appl. Physiol.*, 2010, **109**, 1670–1674.
25 D. Bento, S. Lopes, I. Maia, R. Lima and J. M. Miranda, *Micromachines*, 2020, **11**, 344.
26 D. Bento, L. Sousa, T. Yaginuma, V. Garcia, R. Lima and J. M. Miranda, *Biomed. Microdevices*, 2017, **19**, 1–10.
27 T. Fu, Y. Ma and H. Z. Li, *AIChE J.*, 2014, **60**, 1920–1929.
28 Z. Li, G. Li, Y. Li, Y. Chen, J. Li and H. Chen, *Proc. Natl. Acad. Sci. U. S. A.*, 2021, **118**, 1–6.
29 P. Ma, S. Wang, R. Guan, L. Hu, X. Wang, A. Ge, J. Zhu, W. Du and B.-F. Liu, *Talanta*, 2020, **208**, 120484.
30 R. Abbasi, J. Liu, S. Suarasan and S. Wachsmann-Hogiu, *Lab Chip*, 2022, 994–1005.
31 Z. Liu and X. Lan, *Lab Chip*, 2019, **19**, 2315–2339.
32 K. Raj M and S. Chakraborty, *J. Appl. Polym. Sci.*, 2020, **137**, 1–14.
33 I. Wong and C. M. Ho, *Microfluid. Nanofluid.*, 2009, **7**, 291–306.
34 M. Held, C. Edwards and D. V. Nicolau, *Fungal Biol.*, 2011, **115**, 493–505.
35 I. Miranda, A. Souza, P. Sousa, J. Ribeiro, E. M. Castanheira, R. Lima and G. Minas, *J. Funct. Biomater.*, 2021, **13**, 2.
36 X. Q. Brown, K. Ookawa and J. Y. Wong, *Biomaterials*, 2005, **26**, 3123–3129.
37 R. N. Palchesko, L. Zhang, Y. Sun and A. W. Feinberg, *PLoS One*, 2012, **7**, 1–13.
38 T. L. Poepping, H. N. Nikolov, M. L. Thorne and D. W. Holdsworth, *Ultrasound Med. Biol.*, 2004, **30**, 1067–1078.
39 K. L. Monson, W. Goldsmith, N. M. Barbaro and G. T. Manley, *J. Biomech. Eng.*, 2003, **125**, 288–294.
40 A. Vadapalli, R. N. Pittman and A. S. Popel, *Am. J. Physiol.*, 2000, **279**, H657–H671.
41 P. Angeli and A. Gavriilidis, *Proc. Inst. Mech. Eng., Part C*, 2008, **222**, 737–751.
42 A. J. Calderón, Y. S. Heo, D. Huh, N. Futai, S. Takayama, J. B. Fowlkes and J. L. Bull, *Appl. Phys. Lett.*, 2006, **89**, 244103.
43 D. M. Eckmann, J. Zhang, J. Lampe and P. S. Ayyaswamy, *Ann. N. Y. Acad. Sci.*, 2006, **1077**, 256–269.
44 R. E. Wells and E. W. Merrill, *J. Clin. Invest.*, 1962, **41**, 1591–1598.
45 K. Brookshier and J. Tarbell, *Biorheology*, 1993, **30**, 107–116.
46 T. E. Kornfield and E. A. Newman, *eNeuro*, 2015, **2**, 1–13.
47 F. C. Van Delft, A. S. Perumal, A. van Langen-Suurling, C. De Boer, O. Kašpar, V. Tokárová, F. W. Dirne and D. V. Nicolau, *New J. Phys.*, 2021, **23**, 085009.
48 M. M. Mardanpour, A. S. Perumal, Z. Mahmoodi, K. Baassiri, G. M. Rubies, K. M. LeDez and D. V. Nicolau, In Vitro Investigation of Gas Embolism in Microfluidic Networks Mimicking Microvasculature, *Preprints*, 2022, pp. 1–19, DOI: **10.20944/preprints202203.0193.v1**2022.
49 J. Thaker and J. Banerjee, *Int. J. Multiphase Flow*, 2017, **91**, 63–75.
50 F. Ushikubo, F. Birribilli, D. Oliveira and R. Cunha, *Microfluid. Nanofluid.*, 2014, **17**, 711–720.
51 L. L. Wang, *Front. Phys.*, 2023, **11**, 1125220.
52 D. Grulke, N. Marsh and B. Hills, *Br. J. Exp. Pathol.*, 1973, **54**, 684.
53 J. H. Kennedy, N. H. Hwang, S. G. Von Miller and A. Hartman, *Cryobiology*, 1974, **11**, 483–492.
54 J. L. Smith, D. H. Evans, P. R. Bell and A. R. Naylor, *Stroke*, 1998, **29**, 1133–1138.
55 M. Mastiani, S. Seo, B. Riou and M. Kim, *Biomed. Microdevices*, 2019, **21**, 1–12.
56 R. Gupta, D. Fletcher and B. Haynes, *J. Comput. Multiphase Flows*, 2010, **2**, 1–31.
57 J. Kunes, *Dimensionless physical quantities in science and engineering*, Elsevier, 2012.
58 D. Liu, X. Ling and H. Peng, *Adv. Mech. Eng.*, 2016, **8**, 1687814016637329.
59 I. Frankel and D. Weihs, *Appl. Sci. Res.*, 1983, **40**, 279–294.
60 D. Legendre, R. Zenit and J. R. Velez-Cordero, *Phys. Fluids*, 2012, **24**, 1–12.
61 R. Zhang, F. Tao, H. Jin, X. Guo, G. He, L. Ma, R. Zhang, Q. Gu and S. Yang, *Processes*, 2022, **10**, 799.
62 N.-T. Nguyen, *Micromixers: fundamentals, design and fabrication*, William Andrew, 2011.
63 N. Paiboon, S. Surassmo, U. R. Ruktanonchai and A. Soottitantawat, *Int. J. Multiphase Flow*, 2022, **150**, 104013.
64 N. M. Kovalchuk, M. Sagisaka, K. Steponavicius, D. Vigolo and M. J. Simmons, *Microfluid. Nanofluid.*, 2019, **23**, 1–14.
65 P. M. Korczyk, V. van Steijn, S. Blonski, D. Zaremba, D. A. Beattie and P. Garstecki, *Nat. Commun.*, 2019, **10**, 1–9.
66 C. Brito, J. Graca and P. Vilela, *J. Med. Cases*, 2020, **11**, 394.
67 Y. Huo, G. Finet, T. Lefevre, Y. Louvard, I. Moussa and G. S. Kassab, *J. Biomech.*, 2012, **45**, 1273–1279.
68 A. V. Kamenskiy, J. N. MacTaggart, I. I. Pipinos, J. Bikhchandani and Y. A. Dzenis, *J. Biomech. Eng.*, 2012, **134**, 1–7.
69 J. Bessereau, N. Genotelle, C. Chabbaut, A. Huon, A. Tabah, J. Aboab, S. Chevret and D. Annane, *Intensive Care Med.*, 2010, **36**, 1180–1187.
70 J. Davis and C. Pozrikidis, *Bull. Math. Biol.*, 2014, **76**, 2217–2237.

71 J. B. West, *Respiratory physiology: the essentials*, Lippincott Williams & Wilkins, 2012.
72 F. Lauwers, F. Cassot, V. Lauwers-Cances, P. Puwanarajah and H. Duvernoy, *Neuroimage*, 2008, **39**, 936–948.
73 M. Zamir, *J. Gen. Physiol.*, 1988, **91**, 725–735.
74 A. Etminan, Y. S. Muzychka and K. Pope, *Processes*, 2021, **9**, 870.
75 T. J. Toung, M. I. Rossberg and G. M. Hutchins, *The Journal of the American Society of Anesthesiologists*, 2001, **94**, 360–361.
76 Y. Lee, Y. Wu, W. Gerth and R. Vann, *Undersea Hyperbaric Med.*, 1993, **20**, 289–296.
77 M. S. Jaffee, *Clinical Neurotoxicology*, 2009, pp. 621–628.
78 G. Angles, R. Dotson, K. Bueche and S. C. Pias, *Oxygen Transport to Tissue XXXIX*, 2017, pp. 9–14.
79 D. Gorman, D. Browning, D. Parsons and F. Traugott, *SPUMS J.*, 1987, **17**, 101–115.
80 S. Helps, D. Parsons, P. Reilly and D. Gorman, *Stroke*, 1990, **21**, 94–99.
81 S. Helps and D. Gorman, *Stroke*, 1991, **22**, 351–354.
82 J. Y. Lee and S. J. Lee, *Microfluid. Nanofluid.*, 2010, **8**, 85–95.
83 C. H. Alleyne, C. M. Cawley, G. G. Shengelaia and D. L. Barrow, *Neurosurg. Focus*, 1998, **5**, E2.
84 K. Yoshioka, H. Niinuma, S. Ehara, T. Nakajima, M. Nakamura and K. Kawazoe, *Radiographics*, 2006, **26**, S63–S73.
85 A. Dutka, *Undersea Biomed. Res.*, 1985, **12**, 403–421.
86 P. Sobolewski, J. Kandel, A. L. Klinger and D. M. Eckmann, *Am. J. Physiol.*, 2011, **301**, C679–C686.
87 T. C. Schaefer, S. Greive, C. Bierwisch, S. Mohseni-Mofidi, S. Heiland, M. Kramer, M. A. Möhlenbruch, M. Bendszus and D. F. Vollherbst, *J. Neurointerv. Surg.*, 2023, 1–6.
88 B. Jungwirth, K. Kellermann, M. Blobner, W. Schmehl, E. F. Kochs and G. B. Mackensen, *The Journal of the American Society of Anesthesiologists*, 2007, **107**, 768–775.
89 A. Nozari, E. Dilekoz, I. Sukhotinsky, T. Stein, K. Eikermann-Haerter, C. Liu, Y. Wang, M. P. Frosch, C. Waeber and C. Ayata, *Ann. Neurol.*, 2010, **67**, 221–229.
90 R. A. Van Hulst, J. Drenthen, J. J. Haitsma, T. W. Lameris, G. H. Visser, J. Klein and B. Lachmann, *Crit. Care Med.*, 2005, **33**, 841–846.
91 M. Akcaboy, B. Nazliel, T. Goktas, S. Kula, B. Celik and N. Buyan, *J. Pediatr. Endocrinol. Metab.*, 2018, **31**, 275–281.
92 C.-H. Lee, K.-H. Jung, D. J. Cho and S.-K. Jeong, *BMC Neurol.*, 2019, **19**, 1–7.
93 B. Y. S. Vázquez, *Vasc. Health Risk Manage.*, 2012, **8**, 1.
94 H. H. Billett, *Clinical Methods: The History, Physical, and Laboratory Examinations*, 3rd edn, 1990.
95 I. Badash, D. J. Gould and K. M. Patel, *Front. Surg.*, 2018, **5**, 23.
96 L. Huang, Y. Pan, M. Wang and L. Ren, *Eng. Regen.*, 2023, **4**, 411–426.
97 C. Hall, E. Lueshen and A. A. Linninger, *J. Pharm. Sci.*, 2012, **101**, 1221–1241.
98 P. Hartmann, A. Ramseier, F. Gudat, M. Mihatsch and W. Polasek, *Der Pathologe*, 1994, **15**, 165–170.
99 W. S. Snyder, M. J. Cook, E. S. Nasset, L. R. Karhausen, G. Parry Howells and I. H. Tipton, *Report of the Task Group on Reference Man*, International Commission on Radiological Protection (ICRP), 1974, pp. 1–500.
100 H. Yousefnia, S. Zolghadri, A. R. Jalilian and Z. Naseri, *Journal of Radiotherapy in Practice*, 2015, **14**, 252–259.
101 B. Tufegdzic, M. Lamperti, A. Siyam and F. Roser, *Clin. Neurol. Neurosurg.*, 2021, **209**, 106904.
102 L. A. Tan, K. M. Keigher and D. K. Lopes, *J. Cerebrovasc. Endovasc. Neurosurg.*, 2014, **16**, 93–97.
103 R. Bala and M. Pandia, *Asian J. Neurosurg.*, 2018, **13**, 431–432.
104 D. Celli, J. Galo and C. E. Mendoza, *Cureus*, 2020, **12**, 1–3.
105 M. Nitta, K. Takano and S. Yamanaka, *Intern. Med.*, 2023, **62**, 1311–1317.
106 J. H. Yi, P. J. Choi, J. H. Bang, S. S. Jeong and J. H. Cho, *J. Thorac. Dis.*, 2018, **10**, E59.
107 R. Ramaswamy, K. H. Narsinh, A. Tuan and T. B. Kinney, *Systemic air embolism following percutaneous lung biopsy, Seminars in interventional radiology*, Thieme Medical Publishers, 2014, pp. 375–377.
108 V. Kanchustambham, S. Saladi, K. Mehta, J. Mwangi, Z. Jamkhana and S. Patolia, *Cureus*, 2017, **9**, 1–4.
109 O. Rena, E. Papalia, T. C. Mineo, F. Massera, E. Pirondini, D. Turello and C. Casadio, *Interact. Cardiovasc. Thorac. Surg.*, 2009, **9**, 973–977.
110 A. T. Donato, E. Arciniegas and C. R. Lam, *J. Thorac. Cardiovasc. Surg.*, 1975, **69**, 827–829.
111 A. Bidari and M. Mohamadnejad, *Am. J. Med.*, 2002, **112**, 426–428.
112 Y. Mo, L. Lin, J. Yan, C. Zhong, J. Kuang, Q. Guo, D. Li, M. Wu, Z. Sui and J. Zhang, *BMC Pulm. Med.*, 2021, **21**, 1–6.
113 B. Rylski, F. Mayer, F. Beyersdorf, S. Kondov, M. Kolowca, M. Kreibich and M. Czerny, *Interact. Cardiovasc. Thorac. Surg.*, 2020, **30**, 293–295.
114 G. M. Seong, J. Lee, M. Kim, J. C. Choi and S. W. Kim, *Int. J. Crit. Illn. Inj. Sci.*, 2018, **8**, 176.
115 C.-H. Chang, Y. H. Shin and H.-S. Cho, *Korean J. Anesthesiol.*, 2012, **63**, 72–75.
116 L. O. S. Suastika and Y. H. Oktaviono, *Clin. Med. Insights: Cardiol.*, 2016, **10**, DOI: **10.4137/CMC.S38040**.
117 M. Puthettu, S. Vandenberghe, P. Bagnato, M. Gallo and S. Demertzis, *Cureus*, 2022, **14**, 1–10.
118 R. Nakagawa, T. Nohara, S. Kadomoto, H. Iwamoto, H. Yaegashi, M. Iijima, S. Kawaguchi, K. Shigehara, K. Izumi and Y. Kadono, *IJU Case Rep.*, 2022, **5**, 334–337.
119 S. S.-M. Wong, H. C. Kwaan and T. S. Ing, *Clin. Kidney J.*, 2017, **10**, 797–803.
120 D. Chahal, V. Ruzhynsky, I. McAuley, D. Sweeney, P. Sobkin, M. Kinahan, R. Gardiner and J. Kinahan, *Can. Urol. Assoc. J.*, 2015, **9**, E658.
121 B. Sajid and A. Perumal, *Indian J. Anaesth.*, 2016, **60**, 522–523.
122 G. Lanke and D. G. Adler, *Ann. Gastroenterol.*, 2019, **32**, 156.
123 S. Hynes and R. Marshall, *Can. J. Anaesth.*, 1992, **39**, 748–749.

124 A. A. Zikry, K. DeSousa and K. H. Alanezi, *J. Anaesthesiol., Clin. Pharmacol.*, 2011, **27**, 262.
125 B. D. Spiess, M. S. Sloan, R. J. McCarthy, T. R. Lubenow, K. J. Tuman, S. D. Matz and A. D. Ivankovich, *J. Clin. Anesth.*, 1988, **1**, 25–30.
126 J. B. White, K. R. Thielen and D. F. Kallmes, *Spine*, 2009, **34**, 1526–1528.
127 Z. Patel, R. Sangani and C. Lombard, *Radiol. Case Rep.*, 2021, **16**, 3520–3525.
128 J. Zhang, C. Zhang and J. Yan, *Case. Rep. Neurol. Med.*, 2015, **2015**, 1–4.
129 C. B. Wolff, D. J. Collier, M. Shah, M. Saxena, T. J. Brier, V. Kapil, D. Green and M. Lobo, *Oxygen Transport to Tissue XXXVII*, Springer, 2016, pp. 129–135.